Journal of Ship Research, Vol. 55, No. 1, March 2011, pp. 45–63

A Viscous/Inviscid Interactive Approach for the Prediction of Performance of Hydrofoils and Propellers with Nonzero Trailing Edge Thickness

Yulin Pan and **Spyros A. Kinnas**

Ocean Engineering Group, The University of Texas at Austin, Austin, Texas, USA

A viscous/inviscid interactive (VII) approach is applied to predict the performance of hydrofoils and propellers with nonzero trailing edge thickness. The emphasis has been put on developing VII models for flow separation. The investigation starts from a two-dimensional (2D) hydrofoil. The current method uses an iterative scheme to find a nonlifting closing extension behind the trailing edge. Two kinds of schemes are applied for the iteration process: (1) a non-lifting extension with 1 or 2 degrees of freedom, in fully wetted condition and (2) an extension which is treated like a cavity surface, but with a nonconstant cavity pressure distribution. The results from these schemes are compared with those from a commercial RANS Solver (Fluent). Next, the current schemes using flap extensions are extended to three-dimensional (3D) propeller flows. The 3D models are developed so that all the span-wise strips of the propeller satisfy similar conditions to those used in 2D. A propeller with significant nonzero trailing edge thickness is analyzed, using several 3D models, and the results are compared with existing experimental data.

Keywords: hydrofoil; propellers

1. Introduction

THE BOUNDARY ELEMENT METHOD (BEM) has long been used as an efficient tool for modeling flows around propellers with sharp trailing edges. Coupled with an integral boundary layer solver (XFOIL), viscous effects near the propeller surface can be included. Numerical tools based on this method, such as CAV2DBL (Brewer & Kinnas 1996) and PROPCAV (Kinnas & Fine 1992) coupled with XFOIL, have been found to be robust in predicting the performance of fully wetted or cavitating hydrofoils and propellers. However, real propellers always have finite trailing edge thickness due to many reasons. For example:

- At higher propeller radius, antisinging edges are normally applied, which results in a small finite trailing edge thickness.
- At lower propeller radius, relatively thick or rounded trailing edges are used because of structural reasons. Sharp trailing edges easily get damaged.

No matter what the reason, this feature generates a flow separation zone behind the finite trailing edge, which makes it difficult to apply a boundary element method. Other viscous flow solvers, such as RANS and LES, are more suitable for this type of open trailing edges. [For example, Rhee et al. (2005) applied a RANS solver to a cavitating propeller with closed sections.] However, a fine grid needs to be built downstream of the trailing edge so that the flow downstream of the trailing edge can be modeled. These methods, thus, become too expensive and time-consuming to apply to propeller design. Therefore, it is essential to develop a numerical tool based on BEM, which predicts the performance of hydrofoils and propellers with nonzero trailing edge thickness.

2. Previous work

Experimental evidence (Russel 1958) showed that the separated zone behind the finite trailing edge forms a closed cavity that separates from the potential flow around the propeller. Kudo and Ukon (1994) have developed a three-dimensional (3D) vortex-lattice lifting surface method that solves the steady problem of cavitating propeller with a flow separation zone behind. Their

model assumed the base pressure over the separated zone to be constant and equal to the vapor pressure. Furthermore, Kudo and Kinnas (1995) studied the influence of the length of the separated zone, which affects the pressure and cavity length near the blade trailing edge under fully wetted and partially cavitating conditions. Later, Young and Kinnas (2003) developed a boundary element method to model supercavitating propeller flows using the same assumption. They used a closing rigid extension behind the finite trailing edge and treated the separation zone as an additional cavitation bubble. Their results showed that the geometry of the closing zone does not affect the solution as long as it is inside the supercavity bubble. However, the assumption used in these methods is not accurate enough. Also, these methods fail to apply to fully wetted hydrofoil and propeller flows.

3. Present work

In the present work, more rigorous explanations are developed for the extension, which is used for approximating the flow separation zone. Specifically, the mean closing streamlines after the finite trailing edge are represented by the rigid extension. In two dimensions (2D), different models are established and the results are validated by comparing them with results from Fluent. These models are then applied in three dimensions, with the same assumptions applied on each strip of the propeller blade. The results are compared with experimental data in 3D.

4. Methodology and results for a 2D hydrofoil

4.1. Fluent analysis for a hydrofoil

The flow around a 2D NACA00 hydrofoil ($f_{max}/c = 2\%$; $t_{max}/c = 4\%$, where f_{max} is the maximum camber, t_{max} is the maximum thickness, and c is the chord length), with a vertical cut at 90% chord length (treated as a finite trailing edge) is modeled in Fluent. A fine grid is built around the hydrofoil, especially near the finite trailing edge (thickness = 0.9% of chord length), as shown in Fig. 1. A great effort is taken to build this fine grid to make sure the solution is converged and accurate enough. The Reynolds number is chosen as 10^7 (based on inflow velocity and chord length) and 5 deg angle of attack is used in this case.

The details of numerical schemes used in Fluent simulation are listed in Table 1. Both steady and unsteady cases are run.

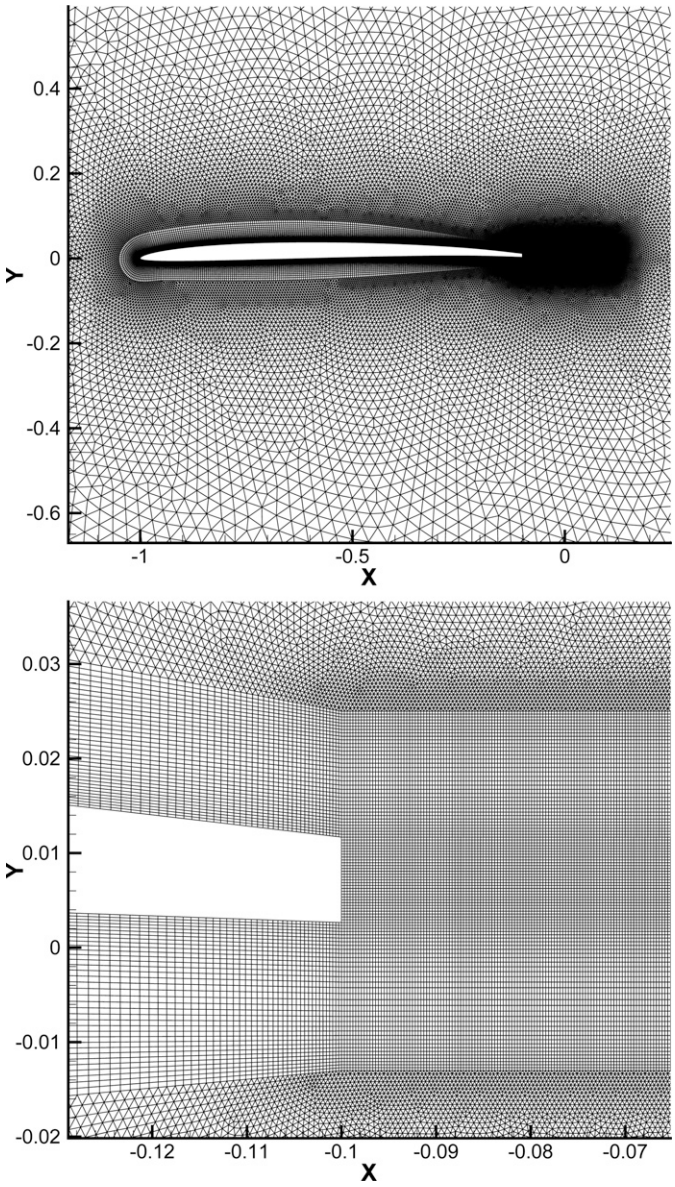

Fig. 1 Grid details near the hydrofoil (top) and near the trailing edge (bottom) used in Fluent (195104 cells in total)

Nomenclature

Aex	= Planform area of a 3D extension (after a strip)	J	= Advance ratio based on V_s, $J = V_s/(nD)$	t	= Time
C_L	= Lift coefficient, $C_L = (\text{Lift})/(0.5 \cdot \rho \cdot U^2 \cdot \text{chord})$ in 2D and $C_L = (\text{Lift})/[(\rho/2)n^2D^2 \cdot Aex]$ for 3D strips	K_Q	= Torque coefficient, $K_Q = Q/(\rho n^2 D^5)$	t_0	= Thickness at trailing edge
		K_T	= Thrust coefficient, $K_T = T/(\rho n^2 D^4)$	T	= Propeller thrust
		n	= Propeller rotational frequency (rev/s)	t_{max}/C	= Maximum thickness to chord ratio
C_p	= Pressure coefficient, $C_p = (P - P_o)/(0.5 \cdot \rho \cdot U^2)$ in 2D and $C_p = (P - P_o)/(0.5\ \rho n^2 D^2)$ in 3D	P	= Pressure	U	= Inflow velocity in 2D
		P_o	= Pressure far upstream, at the propeller axis	V_s	= Ship speed
				u_τ	= Wall shear velocity, $u_\tau = \sqrt{\tau_{wall}/\rho}$
D	= Propeller diameter, $D = 2R$	$P_{0.7}$	= Propeller pitch at 70% of the propeller radius	y^+	= Nondimensional wall distance, $y^+ = u_\tau y/v$
f_{max}/C	= Maximum camber to chord ratio	Q	= Propeller torque	ρ	= Water density
h	= Cavity height	R	= Propeller radius	ϕ	= Perturbation velocity potential
		Re	= Reynolds number	Φ	= Total velocity potential

Table 1 Numerical schemes used in Fluent simulation

Turbulence modeling	Reynolds Stress Model (RSM)
Near wall treatment	Standard wall function
Unsteady formulation	First order implicit in time
Discretization of momentum, turbulent kinetic energy, turbulent dissipation rate, and Reynolds stresses	Second order upwind
Discretization of pressure	Standard
Pressure-velocity coupling	SIMPLE
Residuals	All at 10^{-6}

The unsteady results are time averaged in a vortex shedding period and are found not to be too different from the steady results. The reason that the unsteadiness is not that important is that the vortex shedding is not very strong behind a small finite trailing edge.

The pressure distributions on the hydrofoil and near the trailing edge are shown in Fig. 2. For the sake of explanation, the velocity vectors and the streamlines on the surface of the separation zone are also plotted in Fig. 2*b*, which clearly marks the region of the separation zone. Figure 2*a* shows that the pressure distribution on the upper side and lower side nearly closes at the finite trailing edge. Also, Fig. 2*b* shows that the pressures on the two sides of the surfaces of the separation zone does not change much in the y direction, which excludes the lift on the separation zone. These features of pressure distribution provide the basis of the iteration process coupled in the viscous/inviscid interactive (VII) BEM approach. The closing extension used in the BEM Solver is basically an approximation of the mean separation zone.

As the end of the section of Fluent analysis, the y^+ of the first grid point near the hydrofoil is plotted in Fig. 3. Most of the values fall in a reasonable region for standard wall function. Specifically, (Fluent 2007) suggests that the wall y^+ value should be close to the lower bound of the log-law region ($y^+ \approx 30$) for standard wall functions.

4.2. Viscous/inviscid interactive (VII) BEM approach

4.2.1. VII BEM coupled solver with 1 degree of freedom iteration method. Consider the same hydrofoil used in the Fluent analysis. A closing extension of 10% of the chord length is added behind the trailing edge, and the last camber point on the extension is chosen as the control point (1 degree of freedom) to control the geometry of the extension. The whole extension is generated by interpolation of the original foil and the last point on the extension. By moving the last point up and down, the extension moves like a flapping tail, as shown in Fig. 4.

For the initial solution, the control point is set at an arbitrary vertical position. At each iteration, CAV2DBL (a 2D VII BEM Solver) is used to solve for the pressure distribution on the hydrofoil. This loop continues until a certain convergence condition is satisfied. There are two choices of the convergence conditions:

- Nonlift condition: The lifting force on the extension vanishes.
- Pressure equivalence condition: The pressures at the two sides of the nonzero trailing edge are equal to each other. (Refer to Fig. 2*a*).

The Newton-Secant scheme is used to update the position of the control point at each iteration.

For this case, the convergence criterion is set as $C_L < 10^{-7}$ [$C_L = (\text{Lift})/(0.5 \cdot \rho \cdot U^2 \cdot \text{chord})$] or $\Delta C_p < 10^{-5}$ [The nondimensional pressure C_p is defined as $C_p = (P)/(0.5 \cdot \rho \cdot U^2)$.] Typically, it takes five iterations for nonlift condition to converge and four iterations for pressure equivalence condition to converge, respectively.

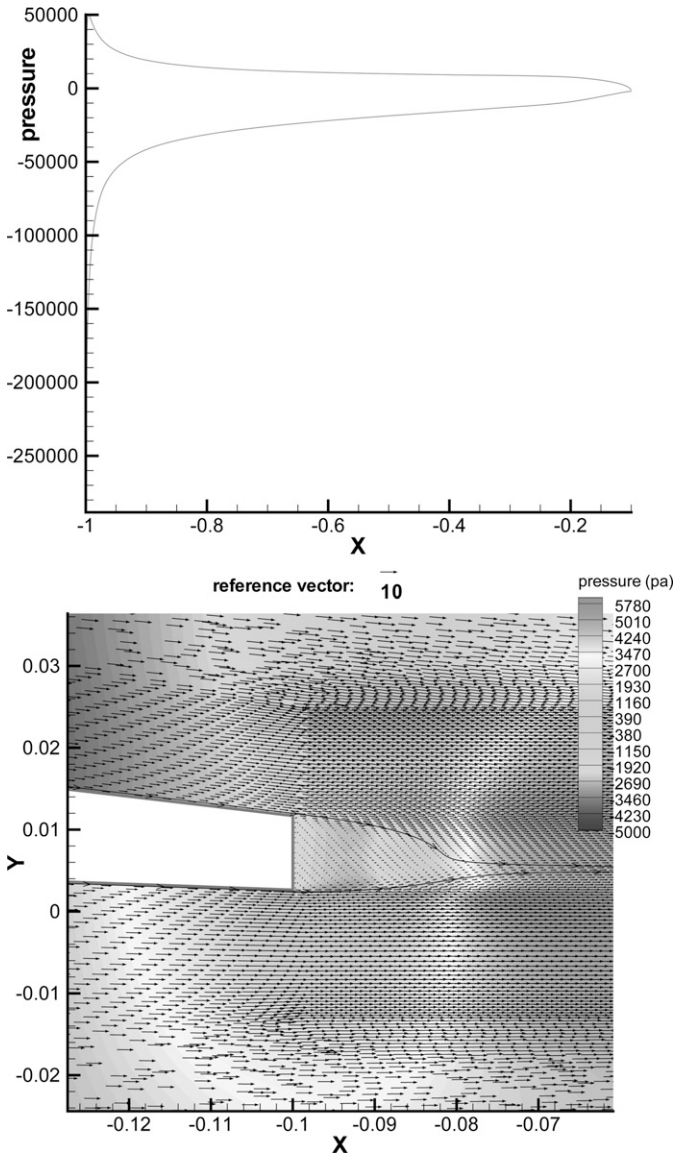

Fig. 2 Pressure distribution (Pascal) from Fluent; (top) on the hydrofoil, (bottom) near the non-zero trailing edge

The pressure distribution on the hydrofoil (by using both conditions) is shown in Fig. 5, with the comparison with Fluent result.

For this geometry, no experimental data are available. However, with sufficient grid resolution, the RANS solver is supposed to model the flow separation with greater accuracy. Therefore, in this comparison, the Fluent result is considered the "correct" result. For the front part of the hydrofoil, the correlation of pressure distribution is good, with only a small difference. Some discrepancy exists near the actual trailing edge for both conditions, but it can be found that the converged results are much better than the initial solution with an arbitrary extension. (Note that in Fig. 5, $x = 0.9$ is the position of the actual trailing edge.)

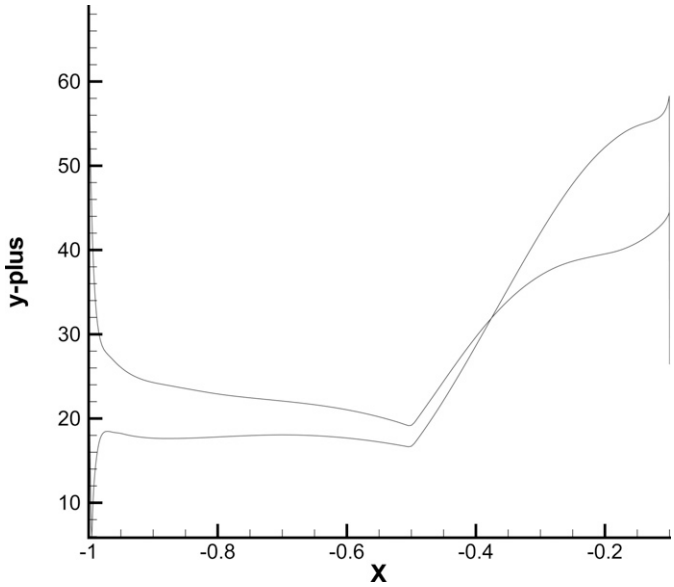

Fig. 3 The values of y^+ of the first grid points near the hydrofoil, using Fluent

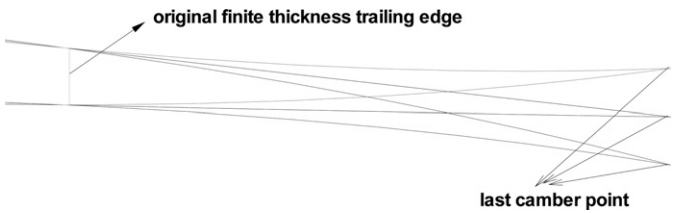

Fig. 4 1 degree of freedom closing extension behind the trailing edge

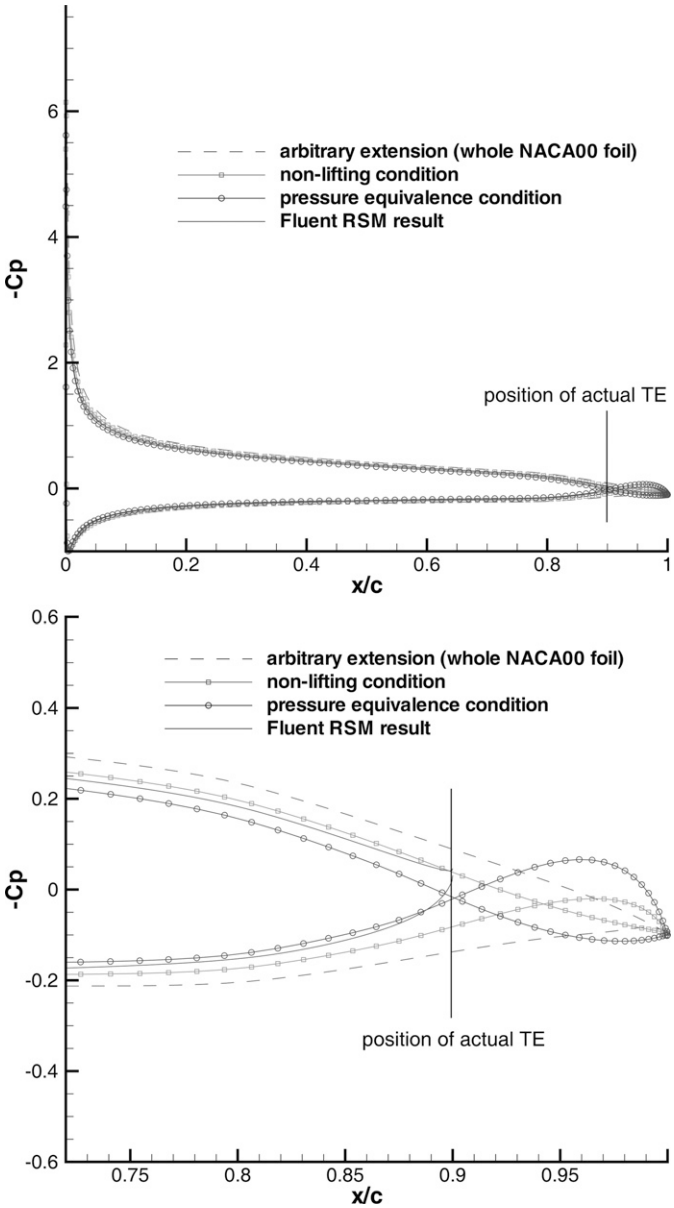

Fig. 5 Comparison of results from the 1 degree of freedom iteration method and Fluent: (top) global result, (bottom) near the trailing edge

However, the nonlift condition and pressure equivalence condition cannot be satisfied simultaneously in 1 degree of freedom iteration method. Both of them have some deficiency when applied separately. Therefore, it is necessary to develop a 2 degrees of freedom iteration method, in which both conditions can be satisfied simultaneously. (Two unknowns are needed for satisfying two conditions simultaneously.)

4.2.2. VII BEM coupled solver with 2 degrees of freedom iteration method. Instead of controlling the extension geometry by using only the last camber point, two camber points on the extension are chosen as the control points (2 degrees of freedom). In this case, the two points are set at $x = 0.93$ and $x = 1$, as shown in Fig. 6. At the end of the iteration process, the two conditions used in 1 degree of freedom iteration method can be satisfied simultaneously. A two-equation Newton-Raphson scheme is used to update the positions of the two control points after each iteration.

In this scheme, we have two unknowns. So the two equations $C_L(y_1,y_2) = 0$ and $\Delta p(y_1,y_2) = 0$ must be satisfied simultaneously. For this case, the convergence criterion is set as $C_L < 10^{-5}$ and $\Delta C_p < 10^{-3}$, and it takes four iterations for the scheme to converge.

The pressure distribution on the hydrofoil is shown in Fig. 7, with the comparison with Fluent result.

As shown in the figure, both conditions used in the 1 degree of freedom iteration method are satisfied. For an arbitrary extension, it affects not only the pressure distribution near the trailing edge, but also the global result. The improvement obtained by applying the 2 degrees of freedom iteration method is significant because it corrects the global result, with only a small discrepancy from the Fluent result near the trailing edge. The correction of the global result is important in evaluation of the lifting force of the whole hydrofoil.

The effect of extension length on pressure distribution is studied, and Fig. 8 shows that its influence on pressure distribution in the front of the trailing edge is negligible. This feature is useful because it allows us to use an extension of arbitrary length within a reasonable range when applying this scheme.

However, a deficiency of this method exists: Even if the lifting force on the extension vanishes, the pressure difference on the two sides at each location is not equal to zero. This is largely due to the

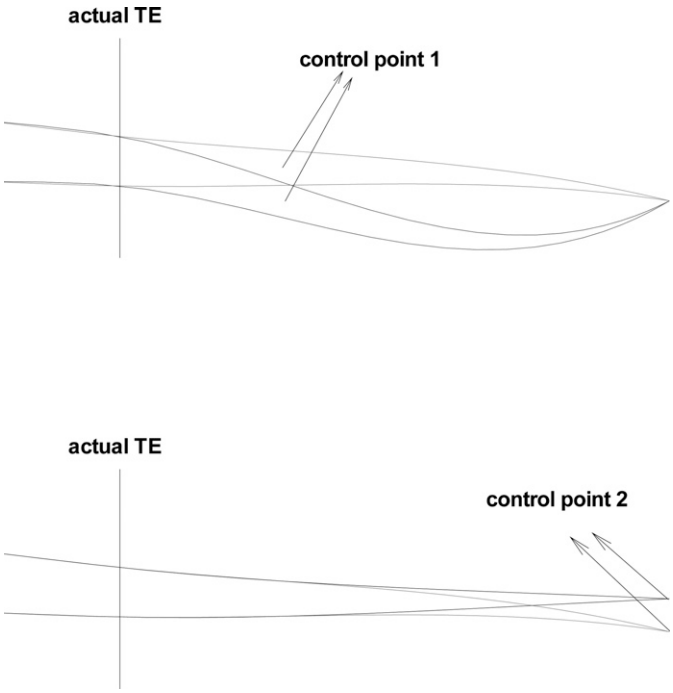

Fig. 6 2 degrees of freedom closing extension behind the trailing edge

insufficiency of the control of the extension geometry in this method. The camber line is controlled by two points, but the thickness form stays unchanged in the iteration process. The scheme described in section 4.2.3 is developed to overcome this difficulty.

4.2.3. Cavity-like scheme. This scheme is developed based on the iteration method for solving partial-cavitating problems. BEM solver has been found to be effective to model partial cavitation on suction side of a 2D hydrofoil (Brewer & Kinnas 1997, Kinnas & Fine 1993). In a cavitation problem, the pressure distribution on the cavity surface is constant. If the two sides of the extension are treated as two cavity surfaces, the scheme will give constant pressure distribution on each side of the extension. Furthermore, if the pressures at the two sides are equal to each other, an extension can be obtained using the condition that the pressure difference at each location is zero. Besides, the previous scheme for cavitation problem can be changed so that different profiles of pressure distributions can be obtained on the extension surfaces.

The mathematical formulation of this scheme is summarized: The perturbation potential, ϕ, must satisfy Green's formula, a Fredholm integral equation of the second kind, on the foil and extension.

$$\pi\phi_p = \int_S \left[-\phi\frac{\partial \ln R}{\partial n} + \frac{\partial \phi}{\partial n}\ln R\right] dS - \int_W \Delta\phi_w \frac{\partial \ln R}{\partial n} dS \quad \text{on S} \quad (1)$$

where S is the surface of the wetted foil and the cavity (extension) surface and W is the surface of the wake. R is the distance from the surface element dS to the point p. $\Delta\phi_w$ is the potential jump in the wake.

On the actual foil and extension, the kinematic boundary condition is satisfied so that the flow is tangent to the surface.

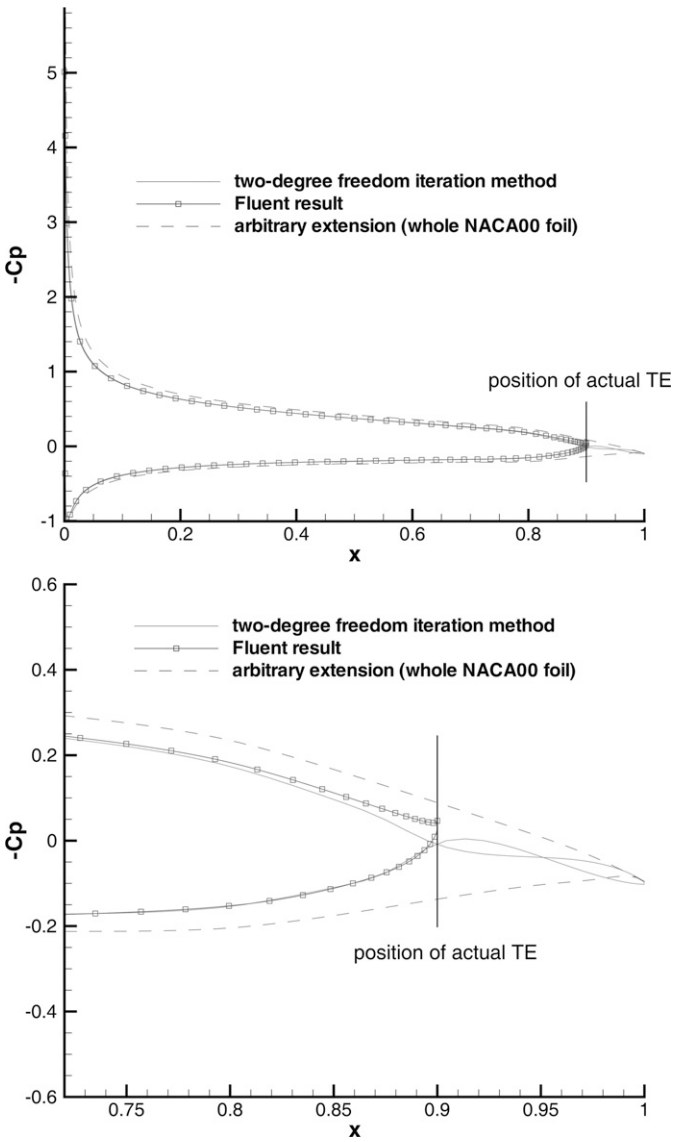

Fig. 7 Comparison of results from the 2 degrees of freedom iteration method and Fluent: (top) global result, (bottom) near the trailing edge

(The cavitation model assumes that the cavity surface is a streamline on which pressure is equal to water vapor pressure.)

$$\frac{\partial \phi}{\partial n} = -\frac{\partial \Phi_{in}}{\partial n} = -U_\infty \cdot \vec{n} \quad (2)$$

On the extension (cavity-like surface), the dynamic boundary condition is satisfied so that the pressure distribution (or velocity distribution) has a certain profile on both sides of the extension.

$$\frac{\partial \phi}{\partial s_{c1}} + \frac{\partial \Phi_{in}}{\partial s_{c1}} = q_{c1}[1 + x \cdot \text{Ratio}] \quad \text{on the upper side} \quad (3)$$

$$\frac{\partial \phi}{\partial s_{c2}} + \frac{\partial \Phi_{in}}{\partial s_{c2}} = q_{c2}[1 + x \cdot Ratio] \quad \text{on the lower side} \quad (4)$$

where Φ_{in} is the inflow velocity potential. s_{c1} and s_{c2} are the arclengths of the suction side extension and pressure side extension, respectively. q_{c1} and q_{c2} are velocities at the leading edges of

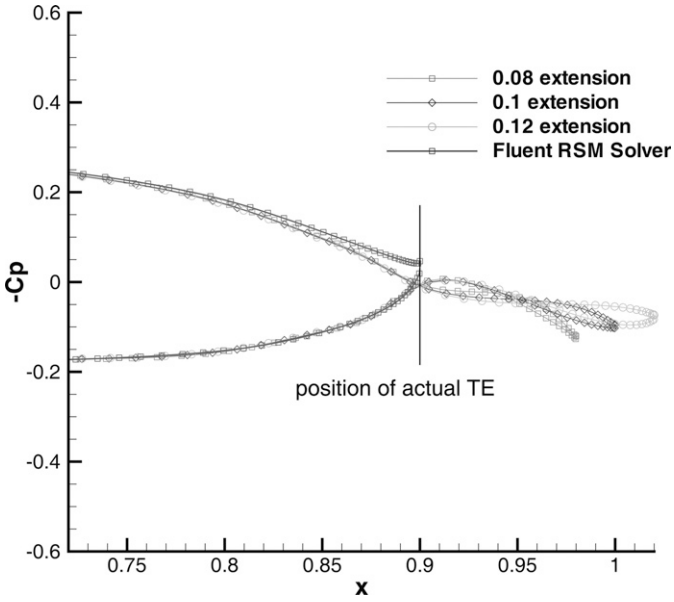

Fig. 8 Influence of extension length on C_p distribution

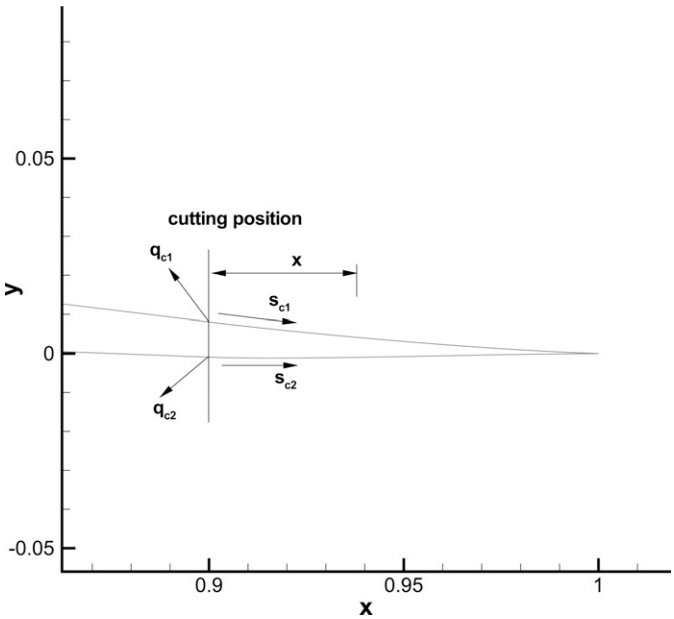

Fig. 9 Definition of variables for cavity-like extension

suction side extension and pressure side extension, respectively. x is the horizontal distance to the finite trailing edge, as shown in Fig. 9. Ratio is set as a user-defined parameter to determine the profiles of pressure distributions on the extension surfaces.

By integrating equations (3) and (4), the expressions for ϕ on the extension are obtained.

$$\phi(s_{c1}) = -\Phi_{in}(s_{c1}) + \Phi_1(0) + q_{c1}\int_0^{s_{c1}} [1 + x \cdot \text{Ratio}]dS \quad (5)$$

$$\phi(s_{c2}) = -\Phi_{in}(s_{c2}) + \Phi_2(0) + q_{c2}\int_0^{s_{c2}} [1 + x \cdot \text{Ratio}]dS \quad (6)$$

where $\Phi_1(0)$ and $\Phi_2(0)$ are the total potentials at the leading edges of suction side extension and pressure side extension, respectively.

The extension surface, and thus s_c, is not known and will be determined iteratively in the present method. As a first iteration, the extension panels are placed on an arbitrary extension behind the finite trailing edge. At each successive iteration, the extension panels are relocated on the updated extension surfaces, which are computed at the end of the previous iteration. The "cavity" height (taken normal to the present iteration "cavity" surface) is h_c, and it represents the amount by which the updated extension surface has to be corrected. At the end of the extension, the cavity closure condition is satisfied so that the cavity height vanishes at the end.

$$h_{c1}(s_{c1_L}) = 0 \quad \text{on the upper side} \quad (7)$$

$$h_{c2}(s_{c2_L}) = 0 \quad \text{on the lower side} \quad (8)$$

where h_{c1} and h_{c2} are the cavity heights on the suction side extension and pressure side extension, respectively. s_{c1_L} and s_{c2_L} are the total arclengths of the suction side extension and pressure side extension, respectively.

It can be shown that the following relationship is valid up to the first order in h_{c1} and h_{c2} (Kinnas & Fine 1991).

$$q_{c1}(1 + x \cdot \text{Ratio})\frac{dh_{c1}}{ds_{c1}} = \frac{\partial\phi}{\partial n} + \frac{\partial\Phi_{in}}{\partial n} \quad \text{on the upper side} \quad (9)$$

$$q_{c2}(1 + x \cdot \text{Ratio})\frac{dh_{c2}}{ds_{c2}} = \frac{\partial\phi}{\partial n} + \frac{\partial\Phi_{in}}{\partial n} \quad \text{on the lower side} \quad (10)$$

Combining Equations (7), (8), (9), and (10), we arrive at the cavity closure condition:

$$\int_0^{s_{c1_L}} \frac{\partial\phi}{\partial n}\frac{ds_{c1}}{1 + x \cdot \text{Ratio}} = -\int_0^{s_{c1_L}} \frac{\partial\Phi_{in}}{\partial n}\frac{ds_{c1}}{1 + x \cdot \text{Ratio}} \quad \text{on the upper side} \quad (11)$$

$$\int_0^{s_{c2_L}} \frac{\partial\phi}{\partial n}\frac{ds_{c2}}{1 + x \cdot \text{Ratio}} = -\int_0^{s_{c2_L}} \frac{\partial\Phi_{in}}{\partial n}\frac{ds_{c2}}{1 + x \cdot Ratio} \quad \text{on the lower side} \quad (12)$$

Equations (1), (2), (5), (6), (11), and (12) can be solved simultaneously for all the unknowns. Suppose we have N panels on the hydrofoil (including the extension), the unknowns to be determined are from $N + 2$ equations. (N equations from Green's formula and 2 cavity closure conditions). Therefore, q_{c1} and q_{c2} are determined in the solution, as well as $\partial/\partial n$ on the foil and extension surface. The updated extension surface is obtained using equations (9) and (10), and the kinematic boundary condition on the extension is only satisfied when the solution of the extension surfaces is obtained. Finally, the pressure distribution is determined on the updated surface, as shown in Fig. 10.

Due to the unsymmetrical geometry of a general foil, the initial arbitrary extension will give some difference between q_{c1} and q_{c2}. To make q_{c1} equal to q_{c2} (so that the two pressures are equal to each other), an outer iteration process is needed (with respect to the inner iteration process to determine the extension surfaces). The last camber point of the extension is again set as the control point, and Newton-Secant method is used to update the vertical position of this point. This outer loop ends until a solution is obtained for which $q_{c1} = q_{c2}$.

A flowchart of the whole process is shown in Fig. 11.

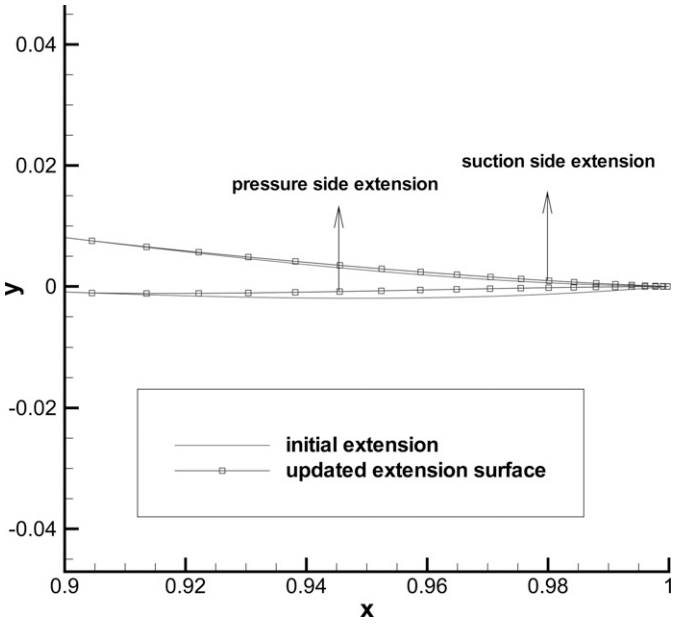

Fig. 10 Updated extension surface

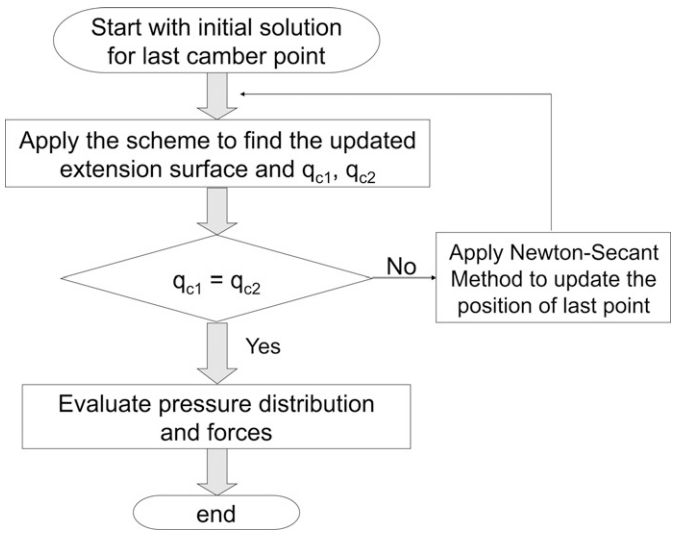

Fig. 11 Flowchart for cavity-like scheme

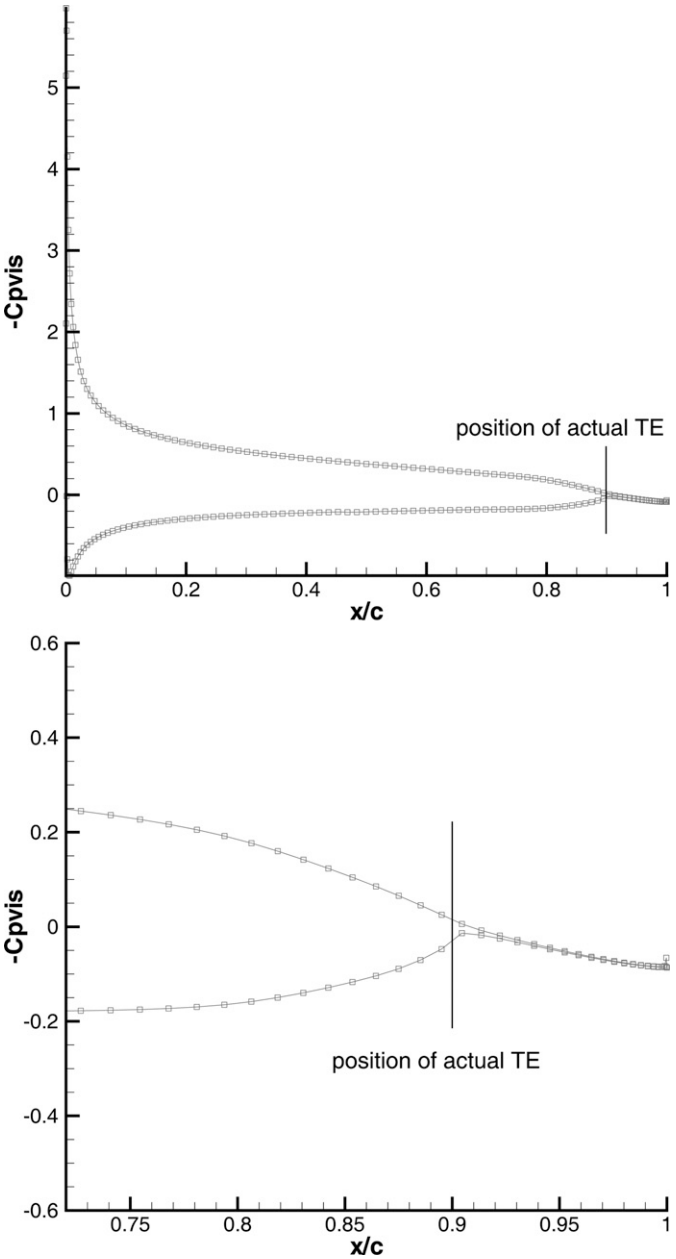

Fig. 12 Viscous C_p distribution on the hydrofoil (Ratio $= -0.3$): (top) global result, (bottom) near the trailing edge

The viscous pressure distribution on the hydrofoil obtained from this scheme for Ratio $= -0.3$ is shown in Fig. 12, from which we can see that the pressure difference at each location on the two sides of the extension vanishes. (Viscous effects influence the pressure distribution so that the differences are not exactly zero at all locations.)

The influence of different values of Ratio on inviscid and viscous pressure distributions is studied in Pan and Kinnas (2009). It is found that the value of Ratio affects the pressure distribution near the trailing edge, but the influence is not significant.

4.3. Correlation of all current methods with Fluent analysis

The comparison of pressure distribution predicted by the current methods and Fluent is shown in Fig. 13, from which one can see that all presented schemes predict the pressure distribution with acceptable accuracy. Also, the 2 degrees of freedom iteration method and cavity-like scheme both give more accurate results, compared with the 1 degree of freedom iteration method, assuming that the Fluent result is the "correct" one.

The comparison of lifting forces evaluated by current schemes and Fluent is shown in Table 2. Note that for the BEM solution, lift is evaluated only over the foil, not including the separation zone. For this case, both the 2 degrees of freedom iteration method and the cavity-like scheme give good correlations with Fluent.

The comparison of computational cost is shown in Table 3, from which we can see that the computational cost is reduced tremendously by applying the presented schemes.

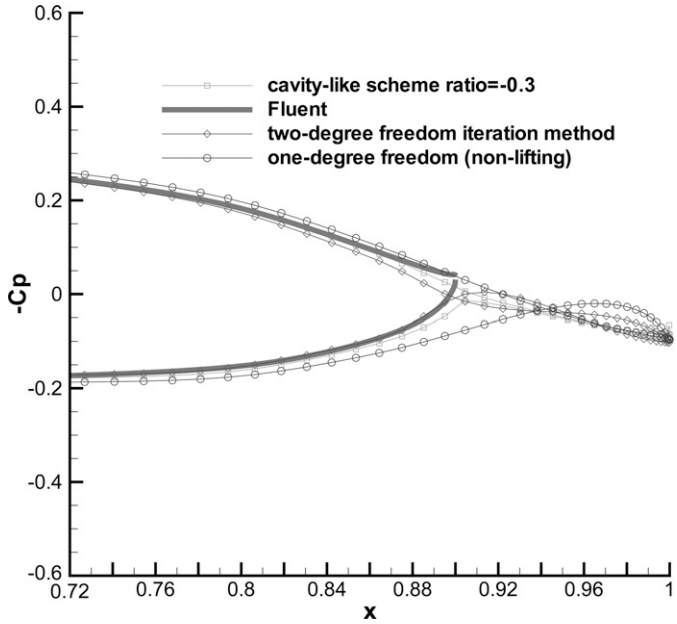

Fig. 13 Comparison of pressure distributions predicted by proposed methods and Fluent at 5 deg angle of attack

Table 2 Comparison of lifting forces predicted by proposed methods and Fluent

Method	C_L
Fluent	0.6717
Arbitrary extension	0.7758
1 degree of freedom	0.7124
2 degrees of freedom	0.6744
Cavity-like scheme	0.6915

Table 3 Comparison of computational cost

Analysis method	Fluent	All presented schemes
Computer characteristics	10 cores of dual-core CPUs (1.6 GHZ AMD Opteron)	1 core of a dual-core CPU
Running time	About 4 hours for steady run	Less than 1 minute

Even though no experimental results are available for this 2D cut foil, it is worthwhile to mention the correlation of BEM/XFOIL model, RANS simulation, and experiment for a closed foil. Brewer and Kinnas (1997) compared the flow property predicted by the BEM/XFOIL model with experimental data, showing that these two agree very well for the fully wetted case. Later Singh (2009) found that the pressure distributions obtained from BEM/XFOIL model and RANS simulation agree very well for a closed NACA00 foil. In conclusion, RANS and BEM/XFOIL models predict the flow very well in the case of a closed foil.

4.4. Results for different angles of attack

Some other results are shown for the same hydrofoil at other angles of attack, for the test of the scheme. Figures 14 and 15 show

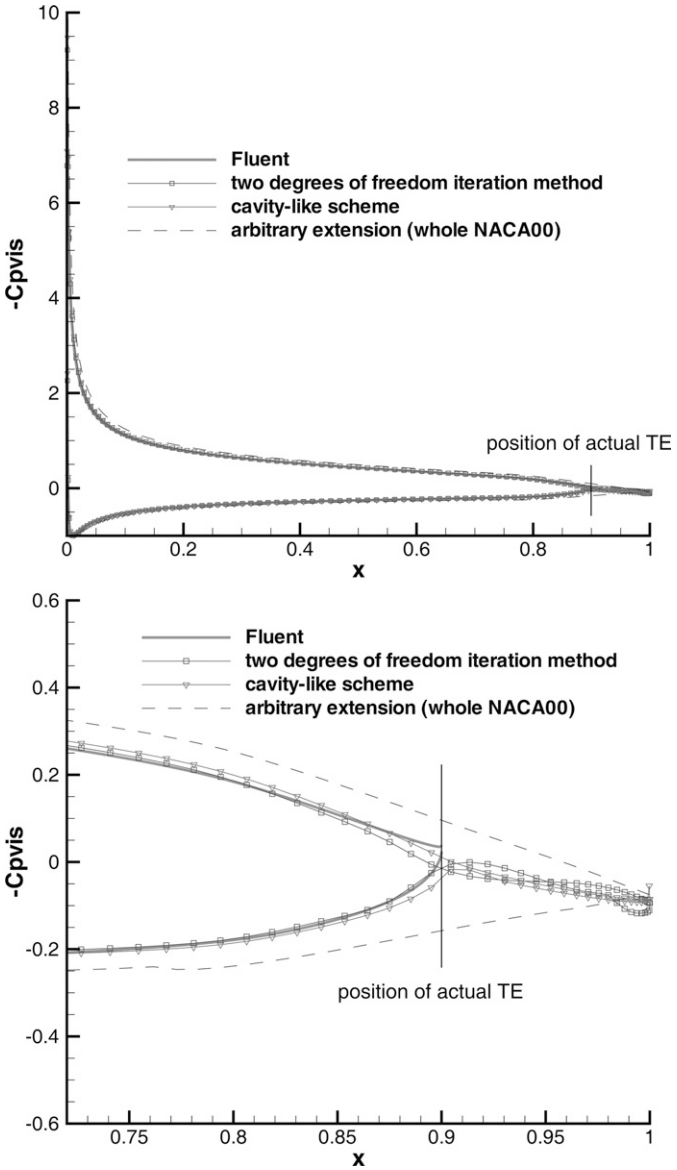

Fig. 14 Comparison of pressure distributions predicted by proposed methods and Fluent at 7 deg angle of attack

the correlations of pressure distributions between current methods and Fluent at 7 and 4 deg angle of attack, respectively. The comparison shows that the 2 degrees of freedom iteration method and the cavity-like scheme both give reasonably accurate results.

5. Methodology and results for a propeller

5.1. Propeller geometry

The propeller used in this study is a five-bladed propeller with $P_{0.7}/D = 0.9288$, where $P_{0.7}$ is the propeller pitch at 70% of the propeller radius, and D is the propeller diameter. A perspective view of the propeller is shown in Fig. 16, and some section geometries of the propeller are plotted in Fig. 17 (only trailing edge parts are shown). More details of the propeller geometry are restricted from inclusion in the paper by the provider of the experimental

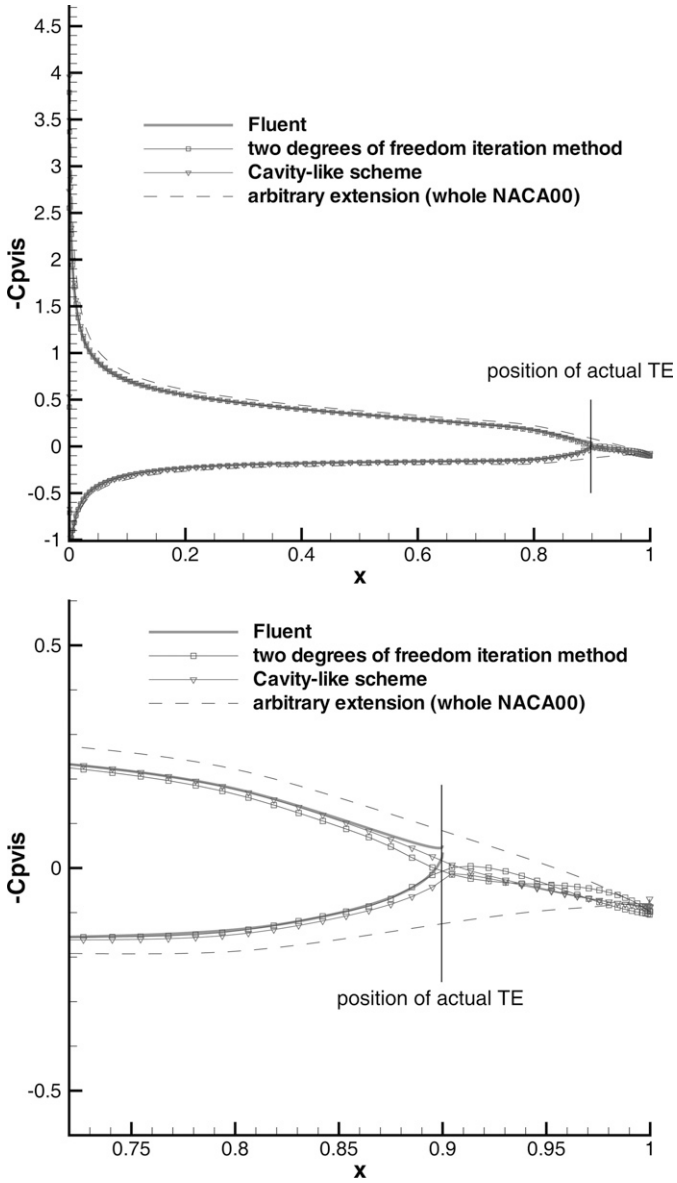

Fig. 15 Comparison of pressure distributions predicted by proposed methods and Fluent at 4 deg angle of attack

data. The feature of this propeller, significant nonzero trailing edge thickness, is evident in both figures. The t_0/c of this propeller varies from 0.6% to 5%, where t_0 and c are the trailing edge thickness and chord length of each strip of the propeller, respectively. For convenience, we will call this propeller "propeller A" hereafter.

In the past, this kind of propeller is treated using an approximation. As shown in Fig. 18, this approximation closes the trailing edge of each strip at its midpoint. In current application, the foil geometries are modified near the trailing edges over 20% of the chord lengths. One way of generating this approximation is by using a parabolic distribution of DS between the original geometry and modified geometry, as shown in Fig. 19. Specifically,

$$DS = (YS_{\text{ori}} - YP_{\text{ori}}) \times (12.5\bar{x}^2 - 20\bar{x} + 8) \tag{13}$$

$$YP_{\text{mod}} = YP_{\text{ori}} + DS \tag{14}$$

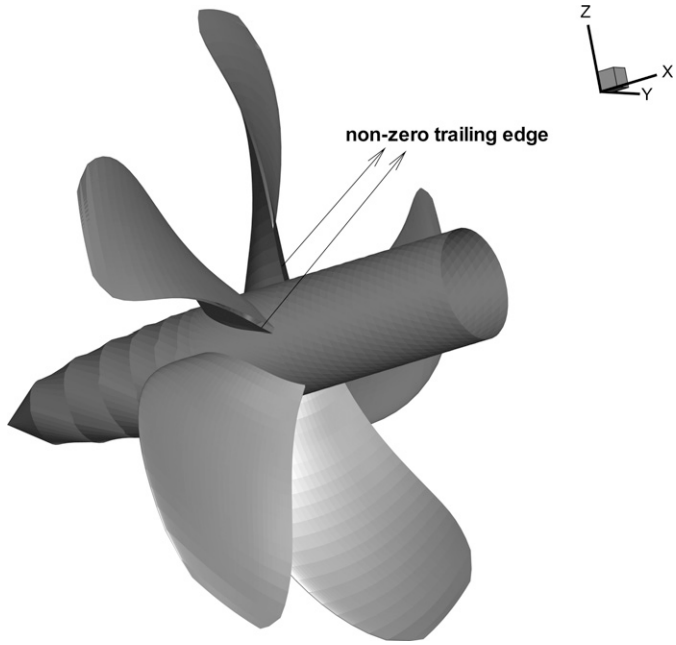

Fig. 16 The propeller A, with significant nonzero trailing edge thickness

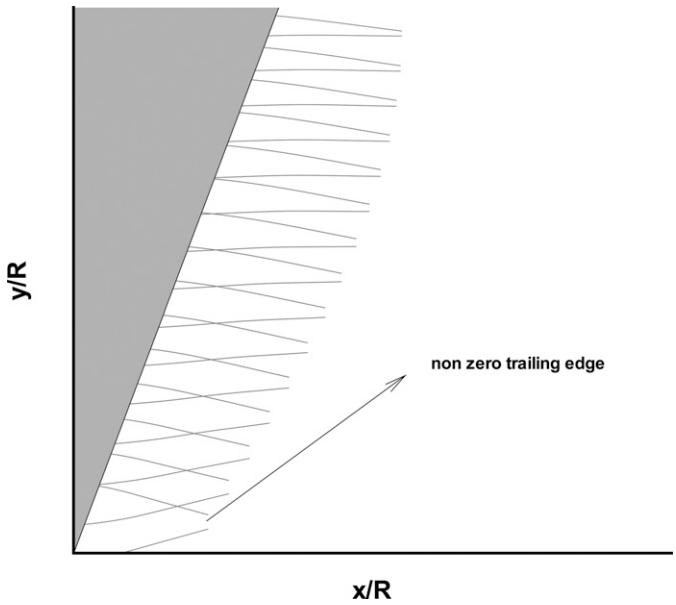

Fig. 17 Expanded view of some sections of propeller A

$$YS_{\text{mod}} = YS_{\text{ori}} - DS \tag{15}$$

$$\text{So that when } \bar{x} = 0.8, YP_{\text{mod}} = YP_{\text{ori}}; YS_{\text{mod}} = YS_{\text{ori}} \tag{16}$$

$$\frac{\partial DS}{\partial \bar{x}} = 0 \tag{17}$$

$$\text{when } \bar{x} = 1.0,\ YP_{\text{mod}} = YS_{\text{mod}} = 0.5 \times (YP_{\text{ori}} + YS_{\text{ori}}) \tag{18}$$

where $\bar{x} = x/c$.

Equation 17 must be satisfied so that the modified geometry does not have a discontinuous slope. On the other hand, different

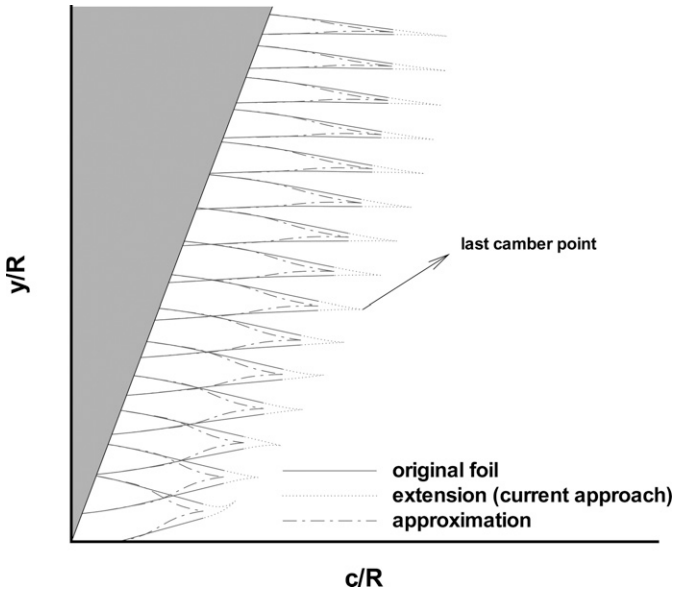

Fig. 18 Approximation used in the past and extensions used in current approach

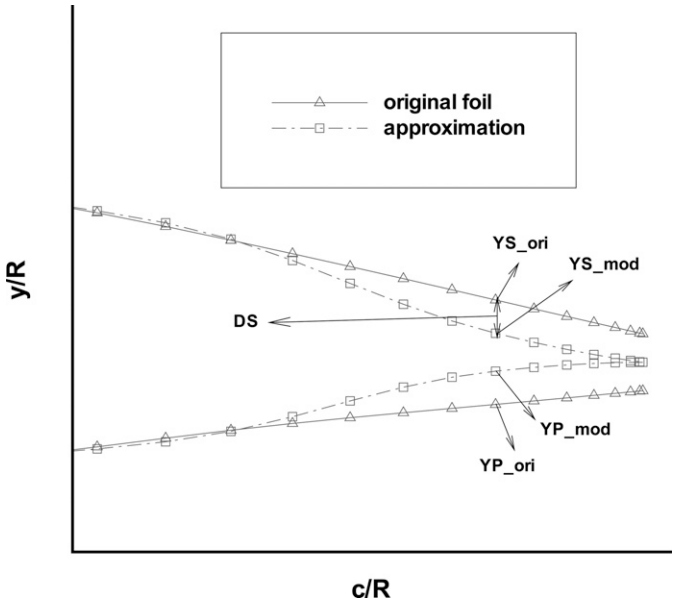

Fig. 19 The way to close the nonzero trailing edge using approximation

lengths of the geometry can be modified by using different variations of DS. In our research, 20% ~40% are tried and it is found that they do not have a significant impact on the forces and moments of the propeller.

In the current approach, we extend each section by a flap, whose geometry is controlled by the location of the last camber point (or two camber points in 2 degrees of freedom model), as shown in Fig. 18. As in the 2D model, we determine the positions of the last camber points so that the conditions used in 2D are satisfied at each strip of the propeller.

5.2. BEM-inviscid model

In this section, the BEM inviscid model is coupled with 1 or 2 degrees of freedom iteration method used in 2D. It turns out that this approach is not able to give a good correlation with experimental data. However, it is necessary to include these results for two reasons:

- Since the convergence of XFOIL is very difficult for some certain geometries in 3D, applying inviscid scheme could prevent this difficulty as a preliminary investigation.
- Convergence study is easier to perform using inviscid model, in which the error from XFOIL is excluded.

5.2.1. One degree of freedom model in 3D. A sample case is provided here, for the explanation of this scheme. Consider propeller A as discussed before; extension of 10% of the chord length (including extension) is added behind each strip. The geometries of the extensions are determined in the same manner as in 2D—by the interpolation of the original strips and the last camber points. For this case, the advance ratio $J = V_s/nD = 0.85$, where V_s is the ship speed, n is the propeller rotational speed, and D is the propeller diameter. 80 (chord-wise) × 20 (span-wise) panels are used, including the extension. Cosine spacing is used in chord-wise, and constant spacing is used in span-wise. Strips 1 to 20 are used for strips from the hub to the tip.

The pressure equivalence condition in 3D is similar to that in 2D. It requires that the 3D pressure distribution closes at the actual trailing edge of each strip. The nonlift condition needs to be performed with more care, in term of the definition of lift. In 3D, each strip sees a different inflow velocity due to the different rotational linear speeds, even if the inflow wake is constant. Therefore, each strip has its own local angle of attack, which is related to the local pitch angle, rotational linear speed, and inflow wake. The nonlift condition in 3D can be expressed as: For each strip, the lift force with respect to the local angle of attack vanishes on the extension. Also, it is worthwhile to mention that the velocity has three components in 3D. The total velocity, including all three components, is considered in the evaluation of pressure using Bernoulli's equation.

Taking pressure equivalence condition as an example, the problem can be described as determining 20 unknowns (positions of 20 camber points y_1, y_2, …, y_{20}) by satisfying 20 conditions (pressure differences at the original trailing edges vanish; Δp_1, Δp_2, …, $\Delta p_{20} = 0$). Mathematically, we need to solve 20 equations:

$$\Delta p_n(y_1, y_2, \ldots, y_{20}) = 0, n = 1, 2, \ldots, 20$$

The solution scheme is described in more details in (Pan 2009).

The convergence criterion is set to $\Delta C_p < 10^{-2}$ $\{C_p = (p - p_0)/[(\rho/2)n^2D^2]$, where p_0 is the pressure at infinity$\}$ for pressure equivalence condition and $C_L < 10^{-3}$ $\{C_L = \text{Lift}/[(\rho/2)n^2D^2 \cdot Aex]$, where Aex is the planform area of the extension and Lift is evaluated by integrating the pressure over the extension of each strip$\}$ for nonlift condition. The converged pressure distributions on different strips are shown in Fig. 20.

As shown in Fig. 20, the nonlift condition or pressure equivalence condition is satisfied on all strips for the two schemes, respectively. For strips near the hub, the correction obtained by applying current schemes is significant, when compared with the

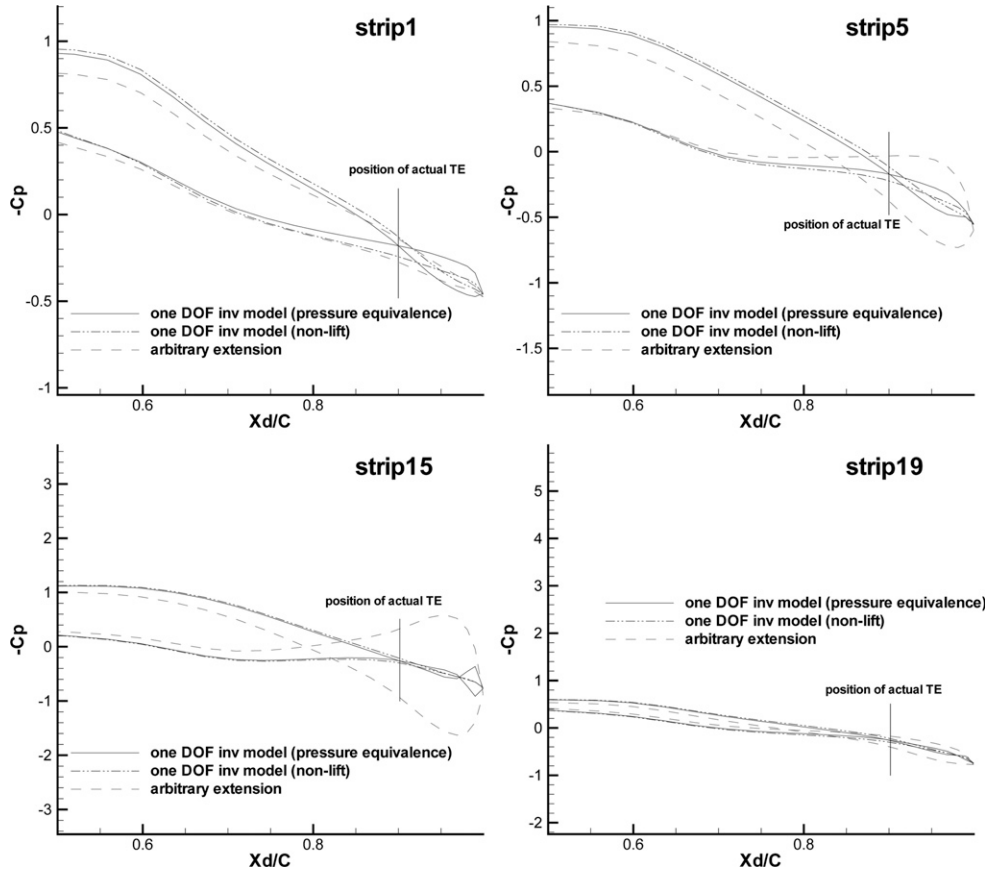

Fig. 20 Inviscid pressure distributions on some sections for 1 DOF model in 3D at $J = 0.85$, span-wise positions of the strips: strip 1: $r/R = 0.1888$; strip 5: $r/R = 0.3552$; strip 15: $r/R = 0.7712$; strip 19: $r/R = 0.9376$

results for arbitrary extensions. This is due to the fact that the trailing edge thickness of the strips near the hub is much larger than those near the tip, as can be seen in Fig. 17.

5.2.2. Two degrees of freedom model in 3D. Another sample case is provided here again, for the sake of explanation. As one DOF model, extension of 10% of the chord length is added behind each strip of propeller A. Instead of controlling the geometry of extension by the last camber point, the midpoint and last point are both chosen as the control points for each strip. For this case, $J = V_s/nD = 0.9$ and 80 × 14 panels are used to discretize the propeller surface. Fewer panels are used in the span-wise direction to have the convergence faster.

The convergence criterion is set the same as the one DOF inviscid model. At the end of the iteration, both conditions should be satisfied for each strip of the propeller, as shown in Fig. 21.

The pressure distributions from the 2 degrees of freedom model do not have too many differences with those obtained by 1 degree of freedom model, except over a small region near the trailing edge. It is found that the forces and moments predicted by these two models are not very different in these 3D applications.

5.2.3. Results. K_T and K_Q predicted by 1 degree of freedom model with both conditions are shown in Fig. 22, with the experimental data and results from the approximation.

As shown in Fig. 22, the 1 degree of freedom inviscid model offers an improvement over using arbitrary extensions. However, it gives no better results than the approximation. Discrepancies with experimental data still exist, especially for K_T. Also, the 2 degrees of freedom model gives results similar to the 1 degree of freedom model as shown (Pan 2009). However, viscous effect is important in this kind of flow separation. Using inviscid model is not supposed to predict the forces and moments well. All the models are developed as viscous models in 2D. The nonlift condition, which we get evidence from Fluent result, only applies to viscous flow. As shown later, applying XFOIL on one DOF model helps improve the results significantly.

One might argue that the 1 degree of freedom inviscid model is no better than using a simple approximation. This is true in terms of inviscid forces and moments. However, using the approximation has two disadvantages:

- Applying XFOIL on the approximated geometry does not help to improve the results, as shown later.
- The modification of the geometry results in significant change of pressure distributions.

Figure 23 shows the pressure distributions at two arbitrary sections by applying the approximation and one DOF inviscid model. Even if the slope of the geometry and pressure distribution are both kept continuous, the results are very different from those obtained by one DOF inviscid model.

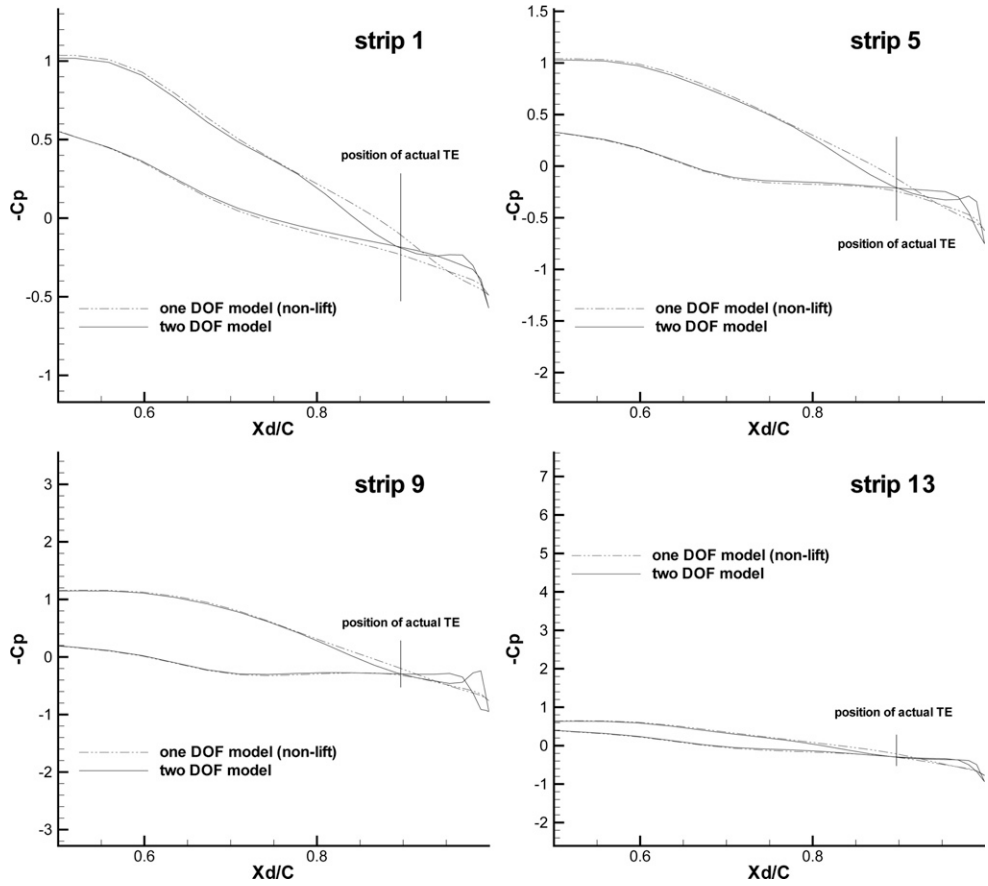

Fig. 21 Inviscid pressure distributions on some sections for 2 DOF model in 3D at $J = 0.9$, span-wise positions of the strips: strip 1: $r/R = 0.1977$; strip 5: $r/R = 0.4354$; strip 9: $r/R = 0.6731$; strip 13: $r/R = 0.9109$

5.3. BEM-viscous model

In this section, XFOIL is coupled with the inviscid solution to obtain the viscous results. In this model, XFOIL is applied on each iteration. In other words, one DOF model is applied on the viscous pressure so that in the end the viscous pressure distribution satisfies the nonlift condition. For example, the propeller A is modeled using 80 × 14 panels. At $J = 0.85$, the pressure distributions on different strips are shown in Fig. 24.

In this case, $Re = 637{,}000$ (based on inflow velocity and propeller diameter), which is set the same as that in the experiment. The predicted K_T and K_Q from this model are shown in Fig. 25. At five different values of J, the current model is applied using 110 × 14 panels. The overall correlation (K_T and K_Q) seems to be the best among all the models, especially for higher values of J, where both K_T and K_Q are improved significantly. Also, applying XFOIL on the approximation fails to give good results, as discussed before.

However, it seems that not much benefit is gained by applying this model at lower values of J. The reason for the discrepancy with the experimental data still needs to be investigated. A possible reason is from the utilized wake alignment model. All the current simulations use a simplified wake model, which aligns the wake geometry with circumferentially averaged inflow (Greeley & Kerwin 1982). This model, called a PSF2-type wake alignment, is not expected to be as accurate for lower values of J. For example, (He & Kinnas 2009) showed that K_T and K_Q predicted using the PSF2-type wake alignment are lower than those from the experiment, as well as those predicted using a complete wake alignment scheme (Lee & Kinnas 2005). Therefore, coupling the current model with the complete wake alignment scheme might help to improve the prediction at lower values of J. This feature is discussed in the next section.

5.4. Influence of wake alignment

For highly loaded propellers, the wake geometry has a large impact on the solution due to the strong vortices shedding from the propeller blade. Using a complete wake alignment scheme (Lee & Kinnas 2005) is essential for an accurate prediction of K_T and K_Q.

Figure 26 shows the inviscid predictions by using both the complete and PSF2-type (Greeley & Kerwin 1982) wake alignment models, with the nonlift modified extension for propeller A. The results show that at lower values of J, the predicted K_T and K_Q are higher when the complete wake alignment is employed. At $J = 0.9$ and $J = 0.95$, the difference between the two wake alignment models is negligible. Therefore, the complete wake alignment is only applied at lower values of J (0.75, 0.8, and 0.85).

The coupling of viscous model and the complete wake alignment scheme is not available in the current work. In order to include the effects of the complete wake alignment on the results, we adjust the predicted K_T and K_Q from the viscous nonlift model

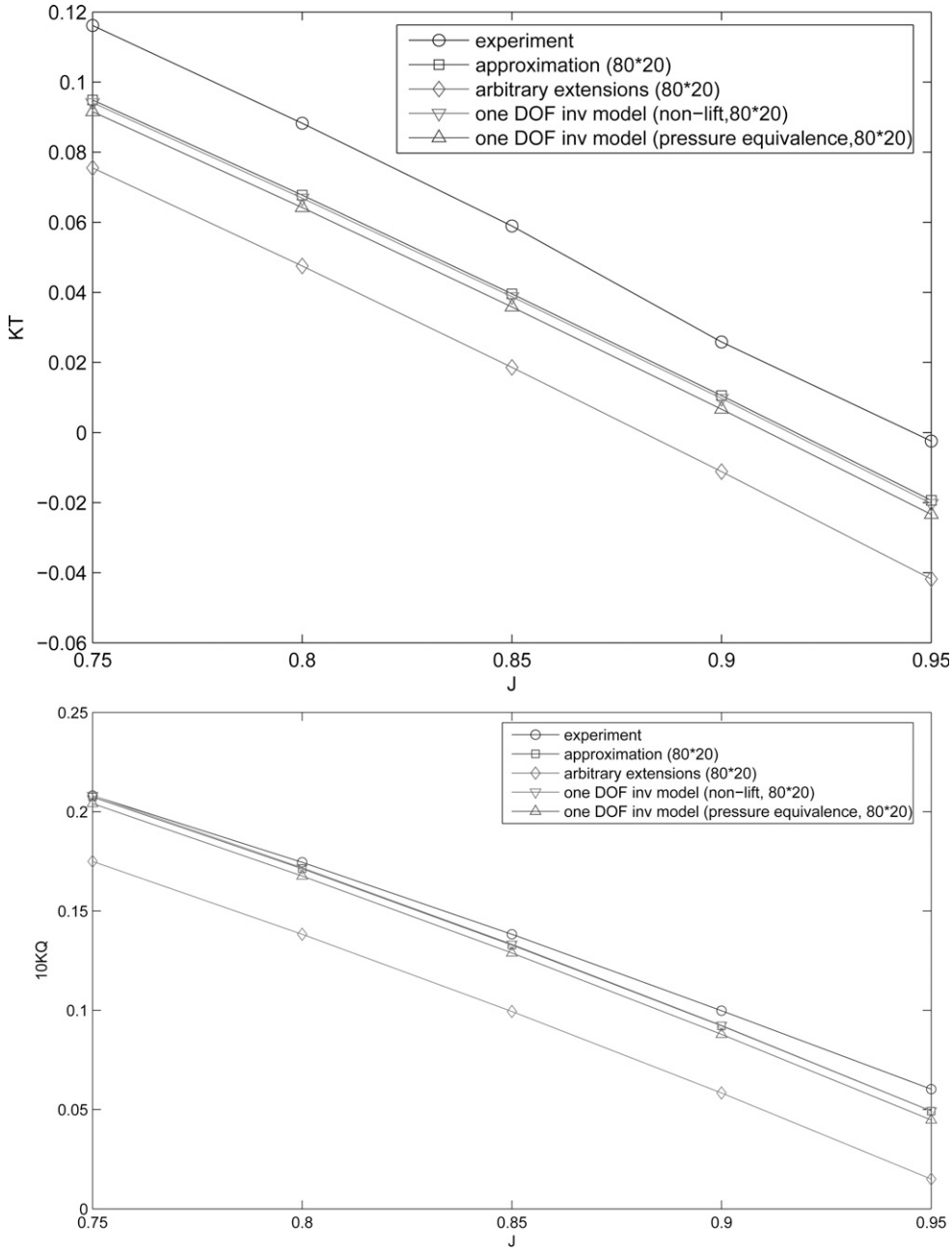

Fig. 22 Results from one DOF inviscid model: (top) K_T, (bottom) K_Q

by the same amount as predicted in inviscid model, as shown in Fig. 27. The correction makes the result closer to the experimental data, with the largest difference within 10%.

In conclusion, the predictions of K_T and K_Q by the viscous nonlift model at lower values of J can be improved significantly by including the effects of complete wake alignment.

5.5. Convergence study

The purpose of the convergence study is to test the convergence of 1 degree of freedom model in 3D. Since applying XFOIL influences the convergence of the result, viscous effects are excluded by using the inviscid results.

For current work, $J = 0.9$ and 80×20 panels are used for propeller A. The one DOF inviscid model with pressure equivalence condition is applied. Other models can be applied using the similar approach.

5.6. Convergence of base pressures with number of chord-wise elements

Evaluating base pressures is a most important issue in current approach. It is worthwhile to study the convergence of base pressures with number of panels.

Figure 28 shows the convergence of base pressures with number of chord-wise elements. The base pressure curve, as

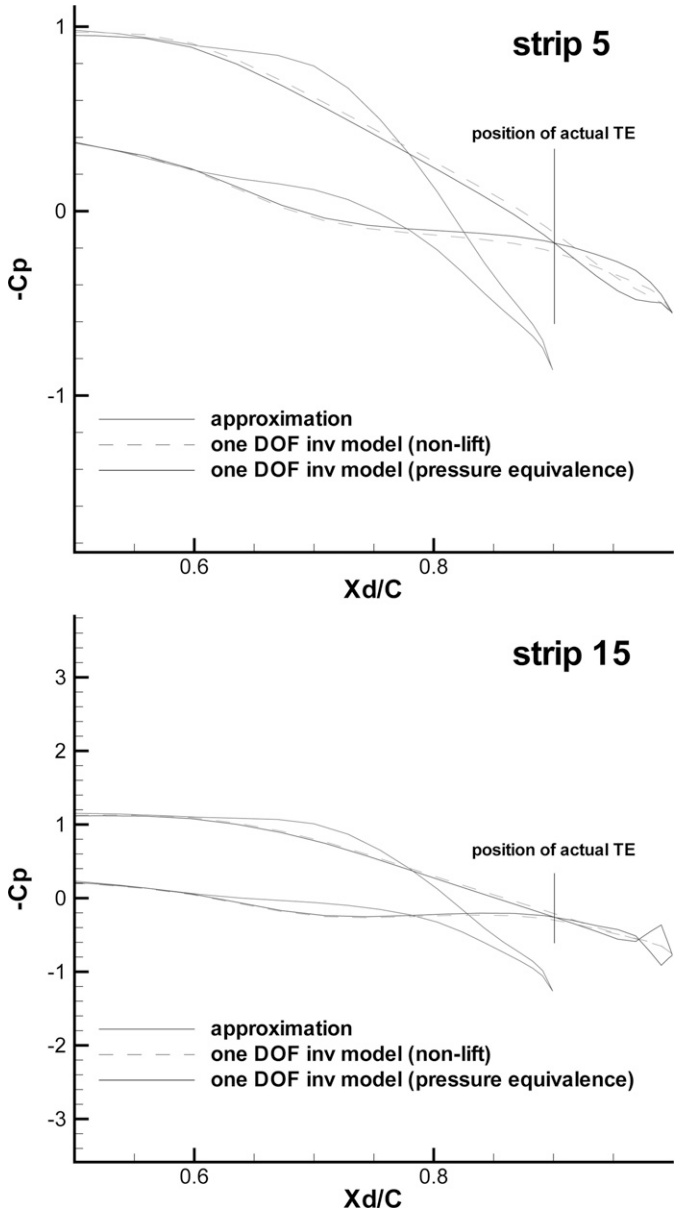

Fig. 23 Pressure distributions on two arbitrary strips from the approximation at $J = 0.85$, span-wise positions of the strips: strip 5: $r/R = 0.3552$; strip 15: 0.7712

shown in the figure, gets converged with increase of number of chord-wise elements. For this case, increasing the number of chord-wise elements reduces the base pressure, but the effect is not significant.

5.7. Convergence of pressure distributions with number of chord-wise elements

The convergence of pressure distributions with number of chord-wise elements is studied. The pressure distributions on three arbitrary strips with different numbers of chord-wise elements are shown in Fig. 29. Since the torque and thrust of the propeller are obtained by integrating the pressure and viscous forces, of which the first part is more important, the convergence of pressure distributions is a good sign on whether the forces and moments converge well.

As shown in Fig. 29, the pressure distributions converge well with increase of number of chord-wise elements. Even though the pressure distributions on the extensions vary with different numbers of elements, the pressures on the actual foil remains the same. (Note that only the pressure distributions from $x = 0$ to $x = 0.9$ are important, not including the extensions.)

More convergence studies with number of chord-wise elements, about the forces and moments, can be found in (Pan 2009).

5.8. Convergence of base pressures with number of span-wise elements

Figure 30 shows the base pressures by using different numbers of span-wise elements at $J = 0.9$. The convergence is good globally except the few strips near the tip. However, this is unavoidable because boundary element method always has a hard time predicting the tip effects of propellers.

5.9. Convergence study of different lengths of extensions

In all the aforementioned cases, extensions of 10% of the chord lengths are used. It is worthwhile to see whether a different length of the extension results in different pressures, forces, and moments. In this study, 80 × 20 panels are used and $J = 0.75$.

Figure 31 shows the pressure distributions on four arbitrary strips of propeller A by using different lengths of extensions. It can be seen that the pressure distributions do not change much on the actual propeller surface, though they vary a lot from one to another on the extension. The K_T and K_Q that result from using different lengths of extensions are shown in Fig. 32. As we expect, the differences among these K_T and K_Q are small, given the small differences in pressure distributions.

From the analysis described in this article, the effects of extension lengths on the pressures, forces, and moments are found to be small. This study is useful because it allows us to use arbitrary lengths of extensions in a reasonable region, without much change of the results.

6. Conclusions

A viscous/inviscid interactive approach and its application to hydrofoils and propellers with nonzero trailing edge thickness were addressed. The investigation started from a 2D hydrofoil. Two kinds of iteration methods were coupled with the VII BEM solver to find a nonlifting extension behind the finite trailing edge, which was used as an approximation of the flow separation zone. The flow around a hydrofoil with nonzero trailing edge thickness was modeled in Fluent and by the current approach. The correlation of the results showed that the current methods provided acceptable results, at a small fraction of the computational cost. The 2 degrees of freedom iteration method and the cavity-like scheme provided more "accurate" results (relative to those from Fluent) than the 1 degree of freedom iteration method in 2D. The 1 and 2 degrees of freedom models were then extended to 3D propeller flows. They were first coupled with the BEM inviscid solution. The predicted K_Q was close to the experimental data, but the predicted K_T was lower. The results were no better than those from an approximation where the aft part of the thickness of the foil is altered so that it closes at the trailing edge. Given that

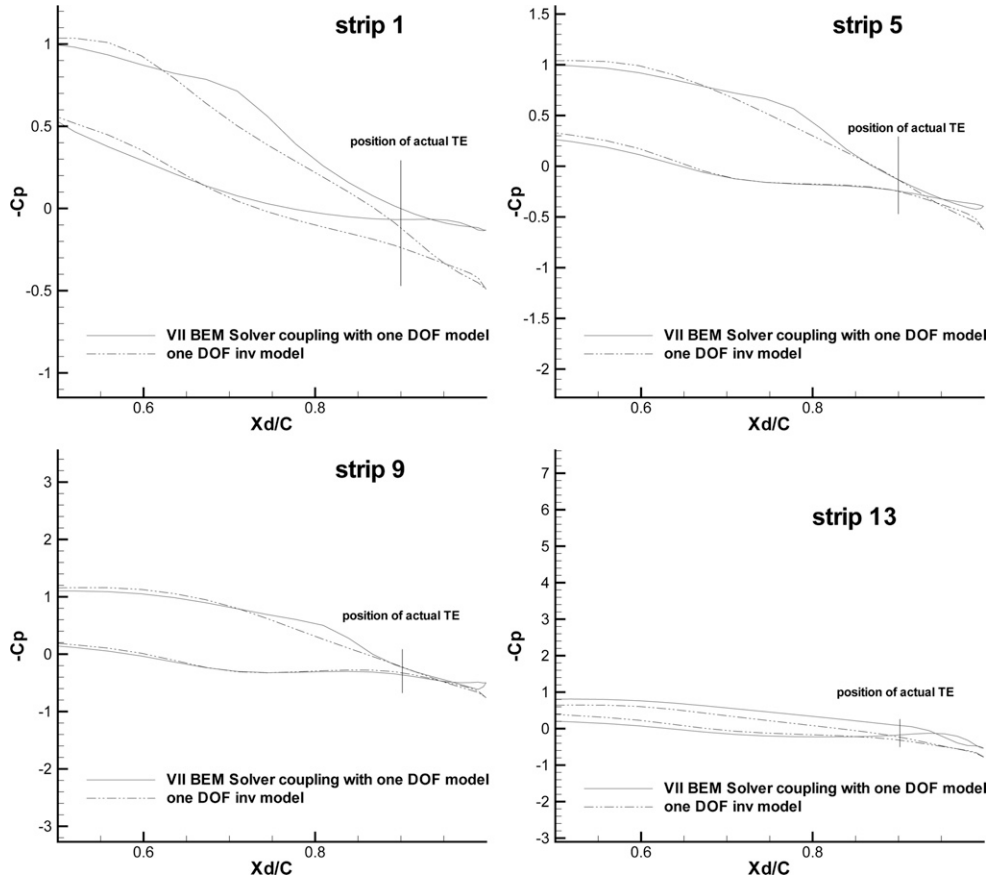

Fig. 24 Pressure distributions by using VII BEM Solver coupling with nonlift condition at $J = 0.85$, 80 × 14 panels are used, span-wise positions of the strips: strip 1: $r/R = 0.1977$; strip 5: $r/R = 0.4354$; strip 9: $r/R = 0.6731$; strip 13: $r/R = 0.9109$

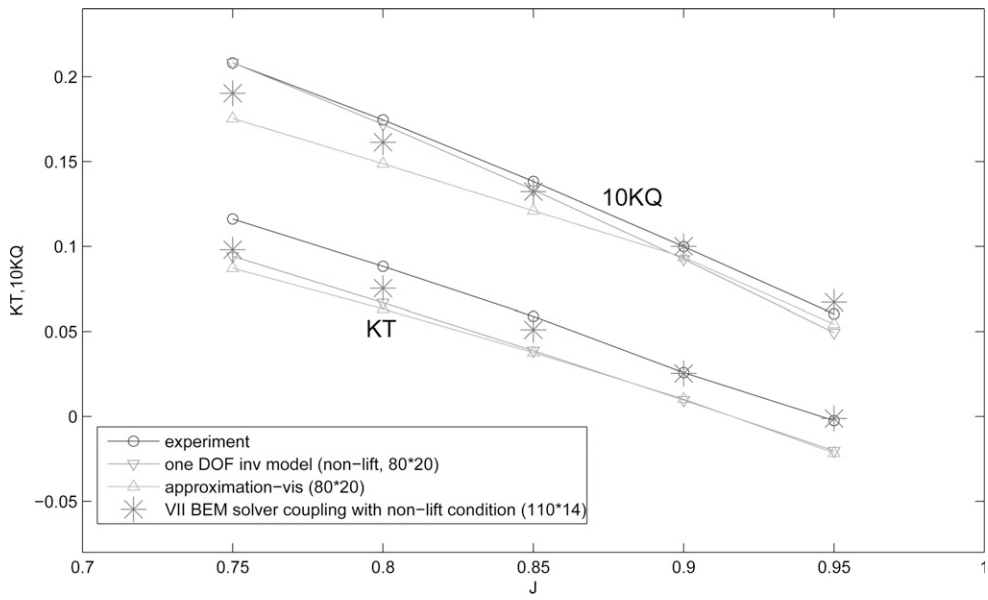

Fig. 25 K_T and K_Q predicted by VII BEM Solver coupling with nonlift condition

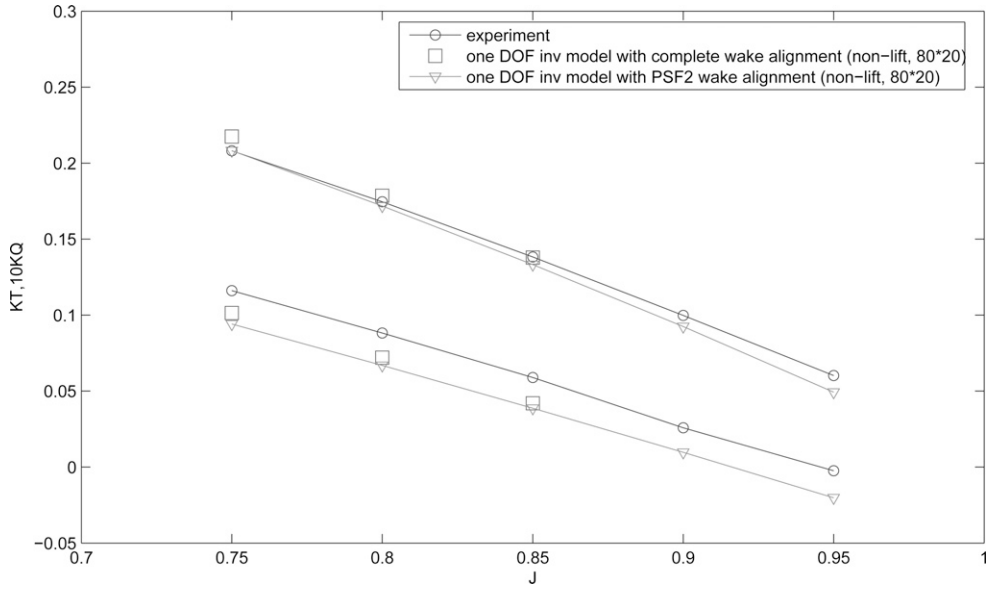

Fig. 26 K_T and K_Q predicted by inviscid nonlift model, with both PSF2-type and complete wake alignment schemes

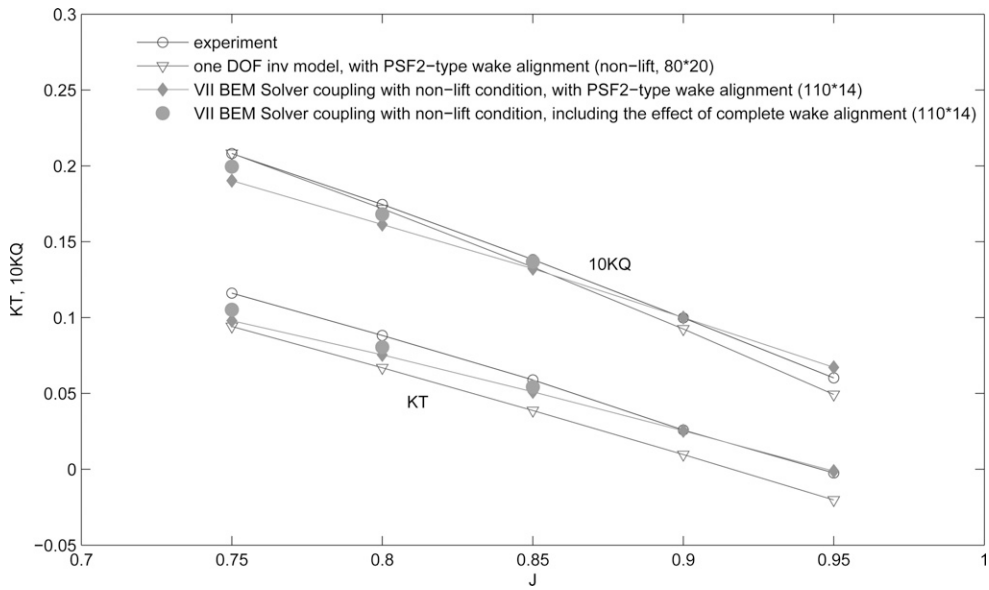

Fig. 27 K_T and K_Q predicted by viscous nonlift model, including the effects of complete wake alignment

viscous effects are important in flow separation, the 1 degree of freedom model with nonlift condition was then coupled with the VII BEM solver, and the results were found to be much closer to those measured.

7. Future Work

We intend to pursue our future research in the following aspects.

- **3D RANS simulation:** It is worthwhile to run a RANS simulation of a realistic propeller with nonzero trailing edge thickness. Detailed 3D flow visualization can reveal the flow property near the separation zone, thus shedding light on improvement of the current model in 3D.
- **Backing condition:** Treatment of backing condition involves flow separation at the rounded "trailing" edge. Applying the current approach might help to overcome this difficulty by using an extension as the approximation of the separation zone.
- **Supercavitation:** Most supercavitating propellers have finite trailing edges. In supercavitation, there are some strips near the hub where only partial cavitation happens. The previous treatment is to use an arbitrary separation zone on which the pressure is set to be vapor pressure, which is nonphysical. The current approach might be able to improve the prediction of performance of super-cavitating propellers.

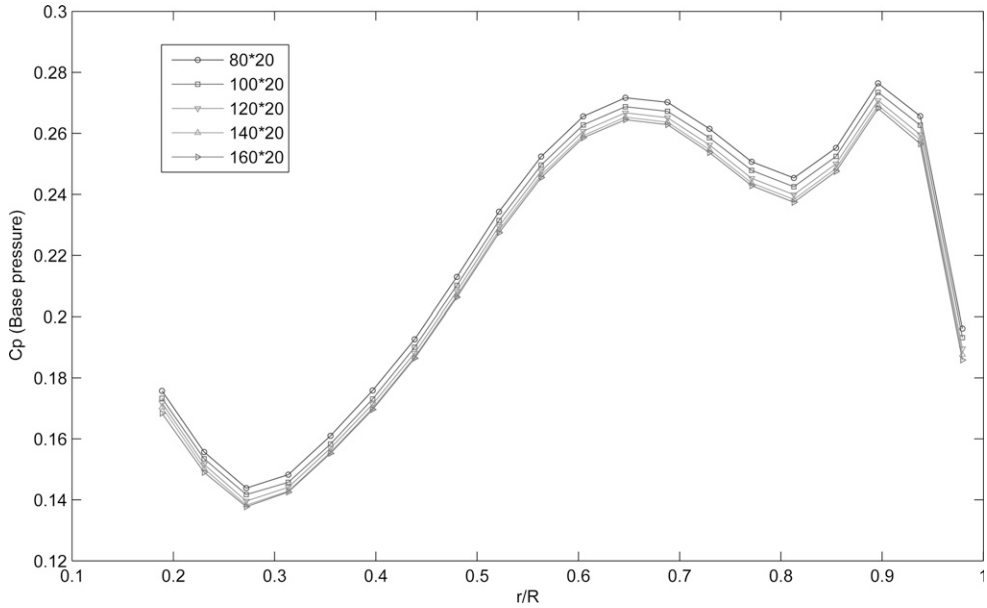

Fig. 28 Convergence of base pressures with number of chord-wise elements at $J = 0.9$, Propeller A

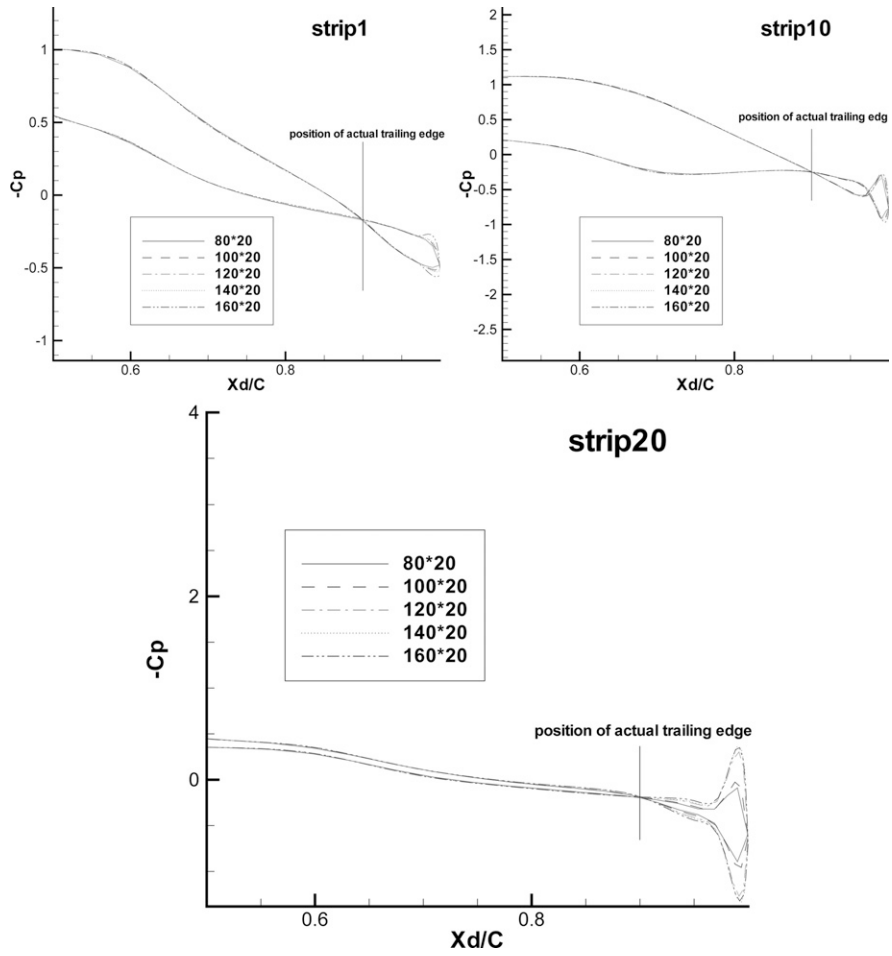

Fig. 29 Convergence of pressure distributions on three arbitrary strips with number of chord-wise elements at $J = 0.9$, propeller A

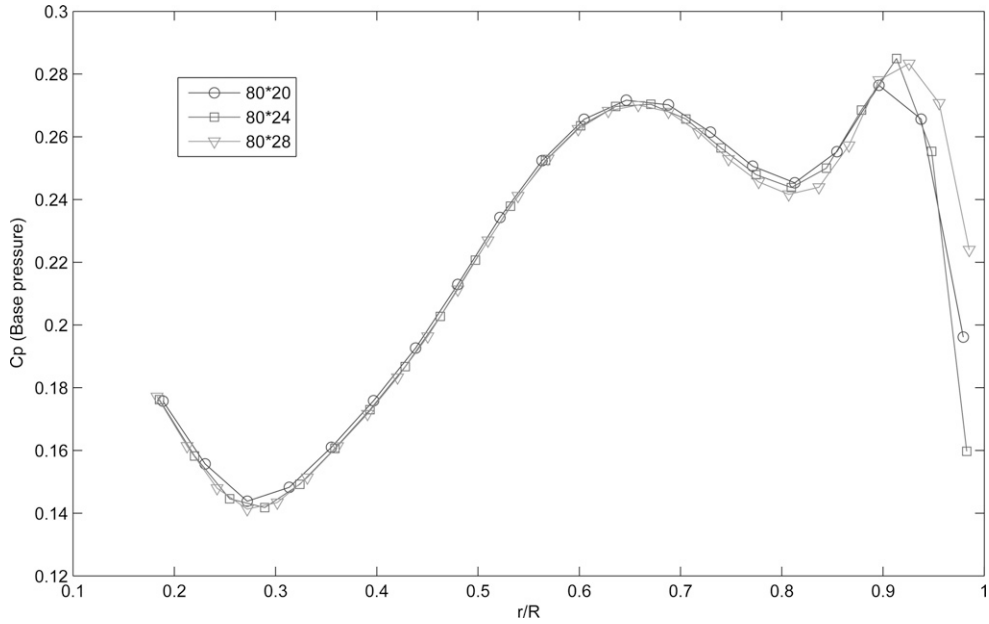

Fig. 30 Convergence of base pressures with number of span-wise elements at $J = 0.9$

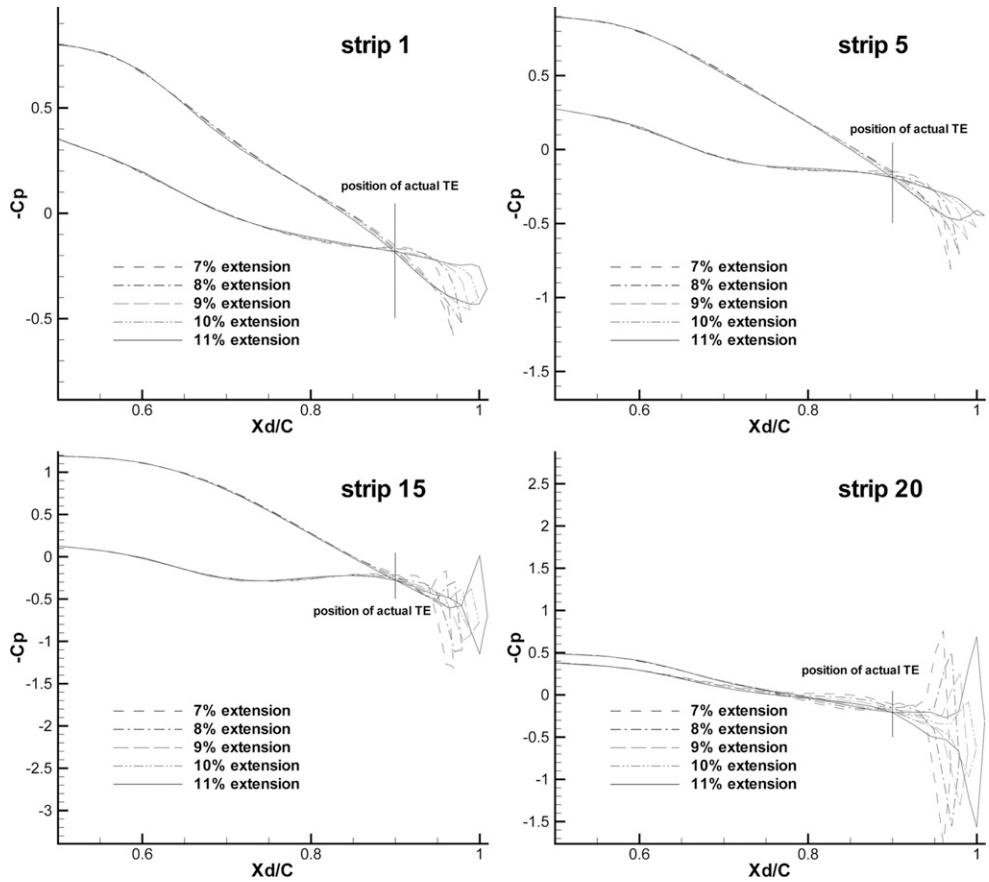

Fig. 31 Pressure distributions on four arbitrary strips of propeller A by using different lengths of extensions at $J = 0.75$, Propeller A, span-wise positions of Propeller A: strip 1: $r/R = 0.1888$; strip 5: $r/R = 0.3552$; strip 15: $r/R = 0.7712$; strip 20: $r/R = 0.9792$

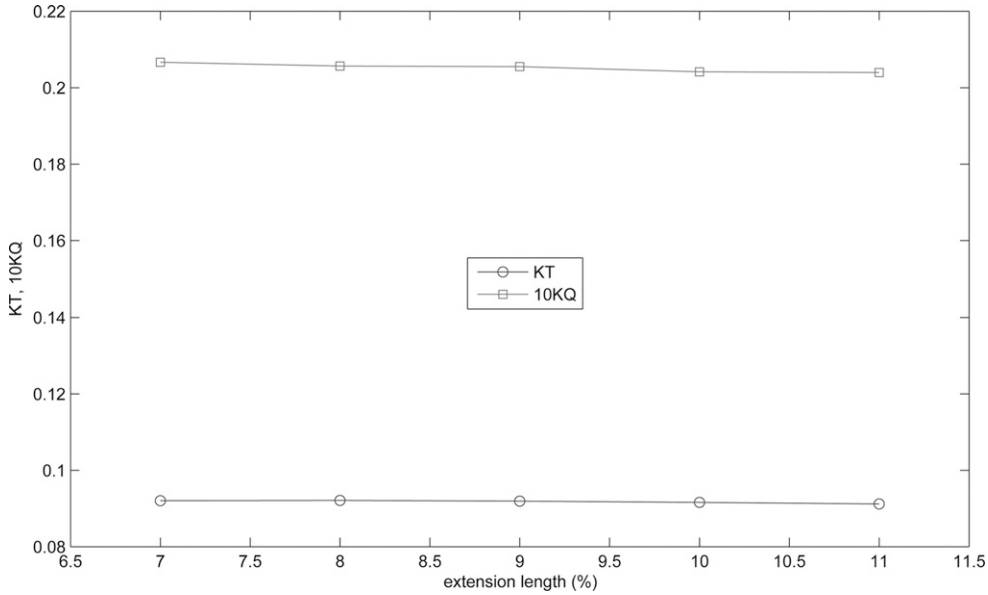

Fig. 32 K_T and K_Q by using different lengths of extensions at $J = 0.75$, Propeller A

Acknowledgments

This work is supported by Phase V of the "University/Navy/Industry Consortium on Cavitation of High Speed Propulsors" with the following members: American Bureau of Shipping, Daewoo Shipbuilding & Marine Engineering Co. Ltd., Kawasaki Heavy Industries Ltd., Naval Surface Warfare Center Carderock Division, Rolls-Royce Marine AB, Rolls-Royce Marine AS, Samsung Heavy Industries Co. Ltd., SSPA AB, VA Tech Escher Wyss GmbH, Wärtsilä Propulsion Netherlands BV, Wärtsilä Propulsion AS, Wärtsilä CME Zhenjiang Propeller Co. Ltd., and Wärtsilä Lips Defense S.A.S. Partial support for this research was also provided by the U.S. Office of Naval Research (contract N00014-07-1-0616).

References

Brewer, W., and Kinnas, S. A. 1996 CAV2DBL (cavitating 2-dimensional with boundary layer) version 1.0. *User's Manual,* Department of Ocean Engineering, Massachusetts Institute of Technology, Cambridge, MA.

Brewer, W. H., and Kinnas, S. A. 1997 Experiment and viscous flow analysis on a partially cavitating hydrofoil, Journal of Ship Research, **41,** 3, 161–171.

Fluent 2007 *6.3 User's Manual,* Fluent Inc., Lebanon, NH.

Greeley, D. and Kerwin, J. 1982 Numerical methods for propeller design and analysis in steady flow. *Transactions—Society of Naval Architects and Marine Engineers,* **90,** 415–453.

He, L., and Kinnas, S. A. 2009 A method for the prediction of rotor/stator interaction-application to 2d hydrofoils and propeller, *Proceedings,* Propeller and Shafting Conference, Williamsburg, VA, September 15–16.

Kinnas, S. A., and Fine, N. E. 1992 A nonlinear boundary element method for the analysis of unsteady propeller sheet cavitation, *Proceedings,* 19th Symposium on Naval Hydrodynamics, August, 717–737.

Kinnas, S. A., and Fine, N. E. 1993 A numerical nonlinear analysis of the flow around 2-d and 3-d partially cavitating hydrofoils, *Journal of Fluid Mechanics,* **254,** 151–181.

Kinnas, S., and Fine, N. 1991 Non-linear analysis of the flow around partially or super-cavitating hydrofoils by a potential based panel method, *Proceedings,* Boundary Integral Methods—Theory and Applications, IABEM-90 Symposium, Rome, Italy, October 15–19, 1990, Springer-Verlag, Heidelberg, 289–300.

Kudo, T., and Kinnas, S. A. 1995 Application of unsteady vortex/source lattice method on supercavitating propellers, *Proceedings,* 24th American Towing Tank Conference, November 2–3, 33–40.

Kudo, T., and Ukon, Y. 1994 Calculation of supercavitating propeller performance using a vortex-lattice method, *Proceedings,* Second International Symposium on Cavitation, April 5–7, 403–408.

Lee, H. and Kinnas, S. 2005 Unsteady wake alignment for propellers in nonaxisymmetric flows. Journal of Ship Research, **49,** 3, 176–190.

Pan, Y. 2009 *A Viscous/Inviscid Interactive Approach and Its Application to Wetted or Cavitating Hydrofoils and Propellers with Non-zero Trailing Edge Thickness,* Masters thesis, The University of Texas at Austin, Dept. of Civil Engineering,. August.

Pan, Y., and Kinnas, S. A. 2009 A viscous/inviscid interactive approach and its application to hydrofoils and propellers with non-zero trailing edge thickness, *Proceedings,* First International Symposium on Marine Propulsors, Trondheim, Norway. June 22–24.

Rhee, S. H., Kawamura, T., and Li, H. Y. 2005 Propeller cavitation study using an unstructured grid based Navier-Stokes solver, *Journal of Fluids Engineering,* **127,** 986–994.

Russel, A. 1958 Aerodynamics of wakes, existence of unsteady cavities, *Engineering,* **186,** 701–702.

Singh, S. 2009 *Viscous/Inviscid Flow around 2-d and 3-d Hydrofoils with Emphasis on Leading Edge Flow Separation,* Masters thesis, The University of Texas at Austin, Dept. of Civil Engineering, August.

Young, Y. L. and Kinnas, S. A. 2003 Numerical modeling of supercavitating propeller flows. Journal of Ship Research, **47,** 1, March, 48–62.